Ceramics International 52 (2026) 10059–10076

Contents lists available at ScienceDirect

Ceramics International

journal homepage: www.elsevier.com/locate/ceramint

Enhanced photoluminescence, thermal stability, and anti-thermal quenching in Li^+/Na^+ Co-doped $K_2B_4O_7:Dy^{3+}$ phosphors for solid state lighting

M.B. Coban [a], Abeer S. Altowyan [b,**], U.H. Kaynar [c,d], Jabir Hakami [e], H. Aydin [f,g], I. Kara [h], A. Canimoglu [i], N. Can [e,*]

[a] Balikesir University, Faculty of Arts and Sciences, Department of Physics, Balikesir, Turkiye
[b] Department of Physics, College of Science, Princess Nourah Bint Abdulrahman University, P.O. Box 84428, Riyadh, 11671, Saudi Arabia
[c] Bakircay University, Faculty of Engineering and Architecture, Department of Fundamental Sciences, Menemen, Izmir, Turkiye
[d] Bakircay University, Biomedical Technologies Design Application and Research Center, Menemen, Izmir, Turkiye
[e] Jazan University, College of Science, Department of Physical Sciences, Physics Division, P.O. Box 114, 45142, Jazan, Kingdom of Saudi Arabia
[f] Central Research Laboratories, Izmir Katip Celebi University, Izmir, Turkiye
[g] Graphene Application&Research Center, Izmir Katip Celebi University, Izmir, Turkiye
[h] Department of Physics, Graduate School of Natural and Applied Sciences, Balikesir University, Balikesir, Turkiye
[i] Omer Halisdemir University, Faculty of Arts and Sciences, Physics Department, Nigde, Turkiye

ARTICLE INFO

Hnadling Editor: Dr P. Vincenzini

Keywords:
$K_2B_4O_7:Dy^{3+}$
Phosphors
Li^+ co-doping
Judd–ofelt analysis
Photoluminescence
Thermal stability
Anti-thermal quenching
CIE chromaticity

ABSTRACT

In this work, Li^+- and Na^+-co-doped Dy^{3+}-activated $K_2B_4O_7$ phosphors were synthesized via a conventional high-temperature solid-state reaction route and systematically investigated. Rather than proposing a universal alkali-ion co-doping effect, this study elucidates a host-specific physicochemical regulation mechanism in the $K_2B_4O_7$ tetraborate lattice, governed by charge compensation and local structural asymmetry. It is demonstrated that $K_2B_4O_7$ can act as an efficient photoluminescent host for Dy^{3+} ions, owing to its wide bandgap, low phonon energy, and structurally rigid tetraborate framework. By introducing Li^+ (or Na^+) as charge compensators for $Dy^{3+}\rightarrow K^+$ substitution, a marked enhancement of emission intensity and thermal stability is achieved. Structural, morphological, and optical characterizations were carried out using XRD, SEM/EDS, FTIR/Raman, and photoluminescence spectroscopy. Under 364 nm excitation, the optimized composition $K_2B_4O_7$:0.03Dy^{3+},0.01Li^+ exhibits intense blue and yellow emissions originating from the $^4F_{9/2} \rightarrow {}^6H_{15/2}$ and $^4F_{9/2} \rightarrow {}^6H_{13/2}$ transitions of Dy^{3+}, together with a high activation energy for thermal quenching ($E_a \approx 0.21$ eV). Concentration-quenching analysis (Blasse and Dexter–Van Uitert models), temperature-dependent PL (300–550 K), and lifetime measurements reveal a pronounced host-dependent anti-thermal-quenching behavior over a wide temperature range (300–550 K), in which the emission intensity increases with temperature due to thermally assisted detrapping and enhanced radiative recombination. Judd–Ofelt analysis further provides quantitative evidence that Li^+ co-doping enhances the local asymmetry and polarizability of the Dy–O coordination environment, leading to strengthened electric-dipole transitions a high internal quantum efficiency (~96.8 %). These results demonstrate a host-tailored quantitative regulation approach based on charge compensation and local-field engineering, highlighting Li^+/Na^+ modified $K_2B_4O_7:Dy^{3+}$ as a thermally robust yellow-emitting phosphor for high-power solid-state lighting applications.

1. Introduction

Borate phosphors have gained significant interest due to their thermal and chemical stability, wide transparency range, and their ability to host a variety of rare-earth ions [1–3]. Within the borate family, tetraborates such as $Li_2B_4O_7$, $LiKB_4O_7$, SrB_4O_7 and CaB_4O_7 are promising photoluminescent hosts because their low phonon energies and rigid frameworks suppress non-radiative relaxation [4–10]. Although

* Corresponding author.
** Corresponding author.
E-mail addresses: asaltowyan@pnu.edu.sa (A.S. Altowyan), ncan@jazanu.edu.sa (N. Can).

https://doi.org/10.1016/j.ceramint.2026.01.181
Received 24 November 2025; Received in revised form 26 December 2025; Accepted 14 January 2026
Available online 17 January 2026

$Li_2B_4O_7$, $LiKB_4O_7$ and SrB_4O_7 have been well studied, $K_2B_4O_7$ remains comparatively unexplored as a photoluminescent host. Its structural similarity to other tetraborates, together with its wide bandgap and low phonon energy, makes $K_2B_4O_7$ a suitable candidate for rare-earth activation. For instance, Dy^{3+}-activated CaB_4O_7, SrB_4O_7 and MgB_4O_7 phosphors have exhibited intense blue and yellow emissions originating from the characteristic $^4F_{9/2} \rightarrow {}^6H_{15/2}$ and $^4F_{9/2} \rightarrow {}^6H_{13/2}$ transitions, highlighting their suitability for white-light-emitting devices [11].

However, unlike these well-studied systems, $K_2B_4O_7$ has so far been explored mainly for thermoluminescence (TL) applications—particularly with Cu, Ag, Mn, and Dy activators [12,13], and systematic photoluminescence investigations remain absent. This research gap is particularly intriguing because $K_2B_4O_7$ combines a stable tetraborate framework with a large bandgap and low phonon energy, potentially providing a favorable environment for RE^{3+} emission centers. Consequently, exploring its photoluminescent properties under Dy^{3+} doping may reveal new opportunities for efficient and thermally stable borate phosphors.

Charge compensation influences the luminescence efficiency by modifying the local symmetry and bonding environment around RE^{3+} ions [14–16]. Incorporation of aliovalent alkali ions such as Li^+ or Na^+ into RE-doped borates has been shown to reduce cation vacancies, induce local lattice distortions, and enhance the electric dipole transition probability [17]. Li^+ co-doping in $Ca_3B_2O_6$:Dy^{3+} phosphors significantly improves the luminescence efficiency by enhancing crystallinity, reducing defect-related non-radiative losses, and optimizing charge balance within the lattice [17]. Similarly, Li^+/Na^+ co-doping in borate hosts promotes charge neutrality and modifies the Dy–O coordination environment, leading to intensified emission and color tunability [10].

In this work, Dy^{3+}-doped $K_2B_4O_7$ phosphors codoped with Li^+ and Na^+ were synthesized using a conventional high-temperature solid-state reaction route. Their structural, morphological and optical properties were characterized by XRD, FTIR and PL measurements. Temperature-dependent PL spectra (300–550 K), together with lifetime measurements and Judd–Ofelt analysis, were used to evaluate thermal quenching behavior, radiative transition probabilities and the local symmetry around Dy^{3+} ions. Alkali-ion co-doping is shown to compensate for the charge imbalance caused by $Dy^{3+} \rightarrow K^+$ substitution, thereby enhancing emission intensity and improving thermal stability. To the best of our knowledge, this is the first detailed photoluminescence investigation of Dy^{3+}-activated $K_2B_4O_7$, providing a foundation for developing thermally robust borate-based phosphors for solid-state lighting applications.

2. Experiment

2.1. Synthesis of $K_2B_4O_7$:Dy^{3+} and Li^+/Na^+ codoped phosphors

The $K_2B_4O_7$:xDy^{3+} and $K_2B_4O_7$:$0.03Dy^{3+}$,yM^+ (M = Li^+, Na^+) phosphors were synthesized by a conventional high-temperature solid-state reaction route. Stoichiometric quantities of analytical-grade K_2CO_3 (99.0 %, Merck), H_3BO_3 (≥99.5 %, Merck), Dy_2O_3 (99.9 %. Merck), Li_2CO_3 (99.9 %, Merck), and Na_2CO_3 (≥99.8 %, Merck) were used as starting materials. Prior to weighing, Dy_2O_3 was pre-heated at 900 °C for 2 h to remove adsorbed moisture and ensure full oxidation. The raw powders were measured according to the nominal compositions and thoroughly ground in an agate mortar for 30–40 min to achieve homogeneous mixing. During this stage, a small amount of ethanol was added intermittently to improve dispersion and minimize agglomeration. The resulting mixtures were transferred into high-purity alumina crucibles and heated in a programmable furnace. The samples were first slowly ramped to 400 °C to allow the complete decomposition of carbonates and boric acid, held for 1 h, and then sintered at 750 °C for 4 h in ambient air. After natural cooling to room temperature, the obtained powders were reground to break up soft agglomerates and stored in airtight containers for further characterization. Dy^{3+} doping levels (x = 0.005–0.07) and alkali-ion co-doping concentrations (y = 0.005–0.07) were adjusted by modifying the corresponding carbonate precursors while maintaining the overall charge balance required for the $K_2B_4O_7$ lattice. No flux or growth promoter was employed, which ensured that any structural or optical variation originated solely from rare-earth or alkali-ion substitution. The final phosphors exhibited stable morphology, phase purity, and good dispersion, suitable for XRD, photoluminescence, and thermally activated emission studies.

2.2. Structural and spectroscopic properties

The structural and spectroscopic examinations of the prepared powders were conducted using a set of standard laboratory instruments. X-ray diffraction patterns were obtained with a Panalytical Empyrean diffractometer operating in Bragg–Brentano geometry, allowing verification of the crystalline phase and the identification of lattice variations associated with Dy^{3+} incorporation and alkali-ion co-doping. The diffraction data were refined by Rietveld analysis to evaluate subtle changes in cell parameters and peak broadening. Vibrational features of the borate host were assessed through Fourier-transform infrared spectroscopy (Thermo Scientific Nicolet iS50), together with Raman scattering measurements acquired on a Renishaw inVia spectrometer using a 532 nm excitation source. These complementary techniques were used to probe BO_3/BO_4 units and to track local modifications around the Dy^{3+} centers. The morphology of the samples was visualized by field-emission scanning electron microscopy (Gemini SEM 500), and elemental composition was examined through the attached energy-dispersive X-ray detector to confirm the presence and spatial uniformity of the dopants. Optical characterizations were performed on an Edinburgh Instruments FS5 spectrofluorometer. Excitation and emission spectra were recorded for all compositions to determine the influence of dopant concentration on spectral evolution. Temperature-dependent photoluminescence measurements were also carried out to evaluate emission stability at elevated temperatures and to identify thermally activated processes. These results, combined with lifetime analysis and Judd–Ofelt calculations, provided a complete picture of the radiative behavior of Dy^{3+} ions in the $K_2B_4O_7$ matrix and the role of Li^+/Na^+ in tuning the optical response.

3. Results and discussion

3.1. Crystal structure and phase purity

Powder X-ray diffraction (XRD) analysis was employed to confirm the phase formation and structural stability of the Dy^{3+}-doped and Li^+/Na^+ co-doped $K_2B_4O_7$ phosphors. The diffraction patterns presented in Fig. 1a show that all the samples—undoped, Dy^{3+}-doped, and Li^+/Na^+ co-doped—are well indexed to the orthorhombic phase of $K_2B_4O_7$ (JCPDS No. 000–2833). The main diffraction peaks corresponding to planes such as (100), (111), (120), (122), (031(220), and (312) are clearly observed without any extra reflections, confirming the phase purity of all compositions. The absence of impurity peaks such as $DyBO_3$, $LiBO_2$, or $NaBO_2$ indicates that both Dy^{3+} and alkali ions have been successfully incorporated into the host lattice without altering its basic crystal structure. The intensity and width of the peaks remain comparable among all doped and co-doped samples, implying that the doping process does not significantly affect the crystallinity or induce major structural distortions.

To further verify the structural parameters and evaluate the effect of doping on the unit-cell dimensions, Rietveld refinement was performed for each composition. The refinement profiles are shown in Fig. 1b, where the observed (I_{obs}), calculated (I_{cal}), and difference (I_{diff}) curves show good agreement. The refined patterns are consistent with the orthorhombic $K_2B_4O_7$ structure (space group *Pba*2). The refinement profiles shown in Fig. 1b exhibit a reasonable agreement between the observed and calculated patterns. Minor residuals are still visible in the

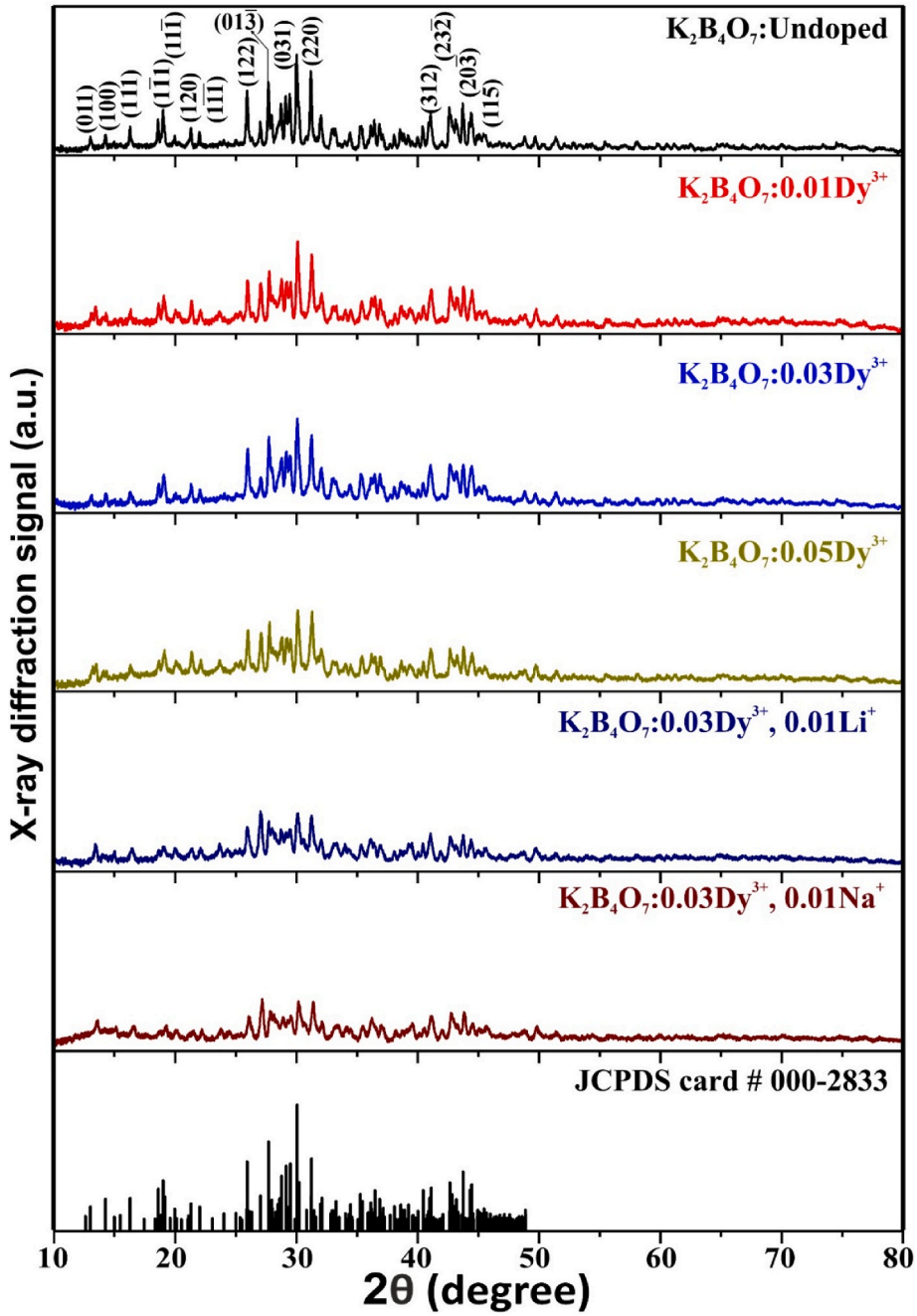

Fig. 1. (a) XRD patterns of undoped, Dy^{3+}-doped, and Li^+/Na^+ co-doped $K_2B_4O_7$ samples indexed with JCPDS card #023–0472; (b) Rietveld refinement profiles of the corresponding compositions; (c) Schematic illustration of the $K_2B_4O_7$ lattice highlighting the polyhedral framework and the substitution of Dy^{3+} ions at K^+ sites. The diagram is intended as a conceptual visualization of the host structure rather than a detailed representation of all dopant species.

difference plots, particularly in low-intensity regions; however, no systematic misfit or unindexed reflections are observed, indicating that the refinement quality is sufficient to confirm phase purity and to discuss relative lattice trends within the detection limits of XRD. The refined lattice constants and reliability factors are summarized in Table 1. The results reveal only minor variations in the lattice parameters with increasing Dy^{3+} concentration or with Li^+/Na^+ co-doping, suggesting that Dy^{3+} ions are incorporated into K^+ sites in the lattice, while charge compensation by Li^+ or Na^+ ions may partially alleviate local lattice distortion around Dy^{3+} centers rather than inducing major structural strain (Fig. 1c). In the $K_2B_4O_7$ host lattice, the incorporation of Dy^{3+} ions is expected to occur predominantly at the K^+ sites due to their similar coordination environment. However, the substitution of Dy^{3+} for K^+ introduces excess positive charge into the lattice, which requires charge compensation to maintain electrical neutrality. This charge imbalance can be accommodated through the formation of potassium vacancies and/or alkali-metal co-doping.

The charge compensation mechanism associated with Dy^{3+} substitution can be described using Kröger–Vink notation as follows:

$$Dy_2O_3 \rightarrow 2Dy_K^{\cdot} + 3O_O^x + 2V_K \quad (1)$$

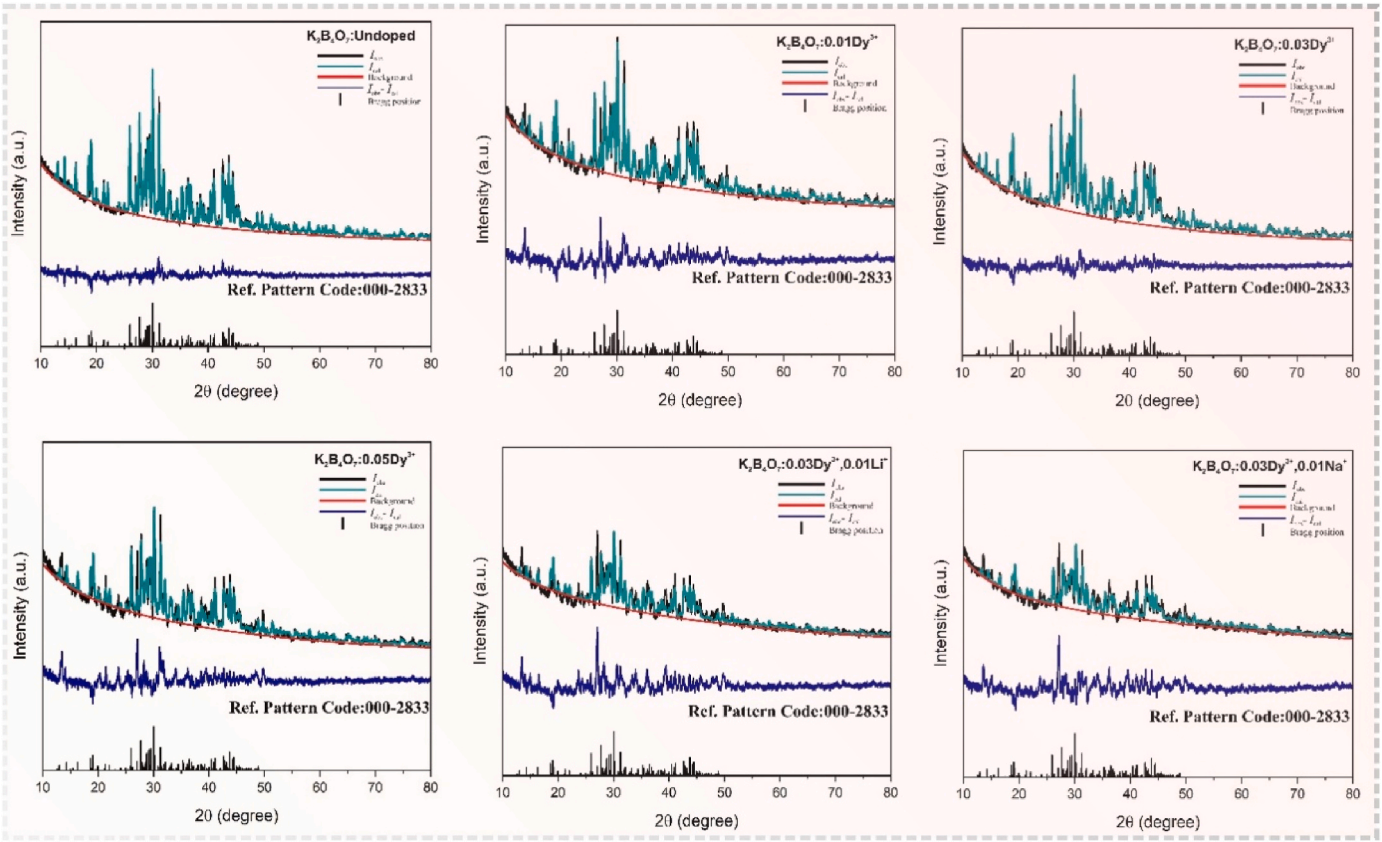

(b)

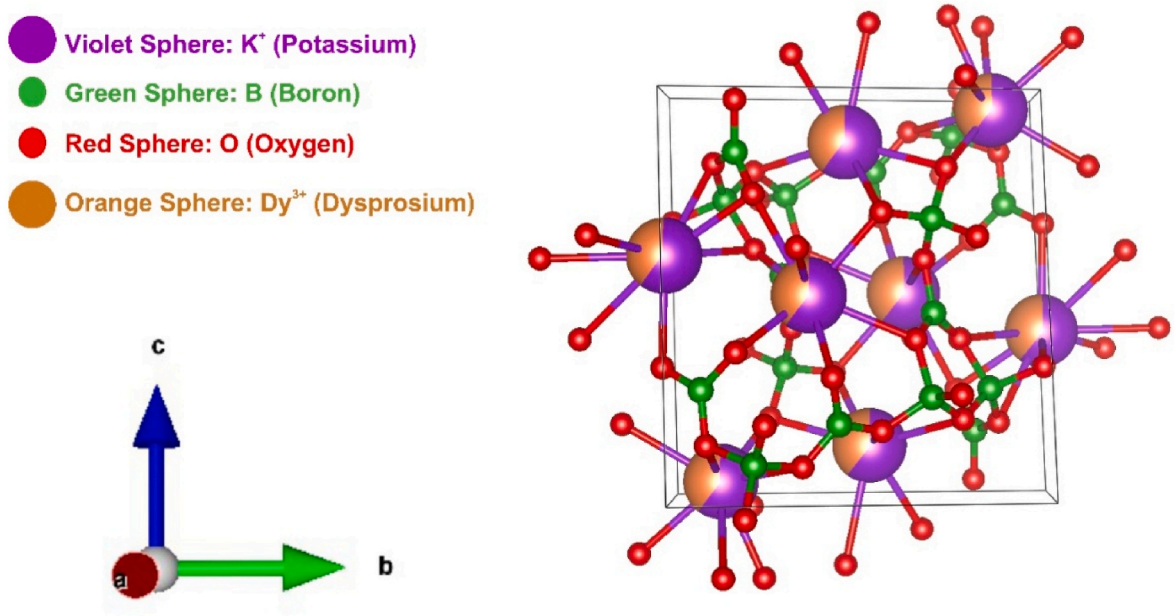

(c)

Fig. 1. (*continued*).

where $Dy_K^{\cdot\cdot}$ represents Dy^{3+} ions occupying K^+ lattice sites with an effective double positive charge, O_O^x denotes oxygen ions located at regular oxygen sites with neutral effective charge, and V_K' corresponds to potassium vacancies formed to compensate the excess charge.

Furthermore, the co-doping of Li^+/Na^+ ions at K^+ sites facilitates charge compensation and may reduce the concentration of potassium vacancies associated with Dy^{3+} substitution. Owing to their smaller ionic radii compared to K^+, Li^+ and Na^+ ions may partially alleviate local lattice distortion around Dy^{3+} centers, rather than inducing

Table 1
Refined lattice parameters (*a*, *b*, *c*), unit-cell volume (*V*), and reliability factors (χ^2, R_p, R_{wp}, R_{exp}) obtained from Rietveld refinement for $K_2B_4O_7$:Dy^{3+} and Li^+/Na^+ co-doped samples.

	$K_2B_4O_7$					
Unit Cell	Undoped	$0.01Dy^{3+}$	$0.03Dy^{3+}$	$0.05Dy^{3+}$	$0.03Dy^{3+}$,$0.01Li^+$	$0.03Dy^{3+}$,$0.01Na^+$
a [Å]	6.48942	6.49123	6.49462	6.49591	6.49631	6.50852
b [Å]	9.61432	9.61346	9.62307	9.62009	9.63093	9.65310
c [Å]	10.41368	10.41141	10.41939	10.41513	10.42735	10.44546
α,*β*,*γ* [°]	89.3,77.2,78.7	89.2,77.2,78.7	89.3,77.2,78.7	89.3,77.2,78.7	89.3,77.2,78.7	89.3,77.3,78.7
Vol. [$Å^3$]	621.1834	621.1372	622.6163	622.2491	623.7808	627.566
χ^2	2.0322	2.0051	1.9553	2.1336	2.4060	2.3506
R_p	0.0423	0.0573	0.0418	0.0608	0.0638	0.0630
R_{wp}	0.0528	0.0743	0.0523	0.0791	0.0834	0.0814
R_{exp}	0.0259	0.0247	0.0267	0.0252	0.0245	0.0243

significant long-range structural strain. This charge-compensation-assisted local structural adjustment provides a favorable local environment for Dy^{3+} luminescence within the $K_2B_4O_7$ lattice. Similar charge-compensation schemes involving alkali-metal co-doping and cation-vacancy formation have been widely reported for Dy^{3+}-doped oxide hosts, where the exact defect configuration depends on the relative ionic radii and valence mismatch between the dopant, co-dopant, and host lattice [18].

The refinement parameters (χ^2, R_p, R_{wp}, R_{exp}) fall within acceptable limits for polycrystalline materials, supporting the reliability of the refinements for comparative structural analysis of the doped systems.

The ionic radius mismatch,

$$D_r = \frac{R_m(CN) - R_d(CN)}{R_m(CN)} \times 100\% \quad (2)$$

was calculated to evaluate the substitutional feasibility of the dopants (see Table 2). The mismatch between K^+ (1.51 Å) and Dy^{3+} (1.027 Å) is ~31.98 %, which is close to the upper limit for effective substitution. Co-doping with Li^+ (0.92 Å) or Na^+ (1.18 Å) significantly reduces local strain by compensating for the charge imbalance and partially offsetting the size disparity. The smaller D_r values for Li^+–Dy^{3+} (10.41 %) and Na^+–Dy^{3+} (14.89 %) indicate better size compatibility and confirm the stabilizing effect of co-doping on the crystal lattice.

3.1.1. Microstructural parameters derived from line broadening analysis

To further investigate the effect of Dy^{3+} and Li^+/Na^+ co-doping on the crystalline size and lattice strain of $K_2B_4O_7$, several classical line-broadening models were applied to the XRD data, including the Debye–Scherrer, Monshi–Scherrer, Williamson–Hall (W–H), Halder–Wagner (H–W), and Size–Strain (S–S) approaches. The calculated results are summarized in Table 3, while the corresponding linear fitting plots are displayed in Fig. 2a–c. According to the Monshi–Scherrer model (Fig. 2a), the average crystallite size increases systematically from ~60 nm for the undoped $K_2B_4O_7$ to ~74 nm for the $K_2B_4O_7$:$0.05Dy^{3+}$ composition. This progressive increase indicates that Dy^{3+} incorporation enhances crystallinity and reduces lattice disorder. For Li^+- and Na^+-co-doped samples, the size values are slightly lower, suggesting that these smaller monovalent ions introduce localized lattice distortions which partially restrict grain growth.

The Williamson–Hall plots (Fig. 2b) show a linear dependence between βcosθ and 4sinθ, indicating that both crystallite size and microstrain contribute to the observed peak broadening. The calculated strain (ε) values range between 2.6×10^{-3} and 3.4×10^{-3}, with a slight decrease at higher Dy^{3+} concentrations, confirming lattice relaxation upon rare-earth incorporation. The Halder–Wagner model (Fig. 2c) yields similar crystallite sizes (60–73 nm) but somewhat higher strain values than those obtained from the W–H method, reflecting its greater sensitivity to broadening effects at small diffraction angles. Finally, the Size–Strain plots (Fig. 2d) confirm the overall consistency of the previous analyses. The strain decreases from 2.3×10^{-3} (undoped) to 1.4×10^{-3} ($0.05Dy^{3+}$), indicating a relaxation of internal stress as Dy^{3+} ions substitute into the K^+ sites. The co-doped systems exhibit slightly higher strain values, likely due to local charge-compensation distortions caused by Li^+ or Na^+. Overall, all models point toward improved crystallinity and reduced microstrain upon Dy^{3+} doping, while Li^+/Na^+ co-doping introduces controlled lattice perturbations that stabilize the crystal structure without inducing phase distortion. These findings agree well with the Rietveld refinement results and XRD phase analysis.

3.2. Microstructural and compositional analysis (SEM–EDS)

The surface morphology and elemental composition of the undoped and Dy^{3+}-doped $K_2B_4O_7$ samples were examined by scanning electron microscopy (SEM) combined with energy-dispersive X-ray spectroscopy (EDS). The obtained SEM micrographs and corresponding EDS spectra are presented in Fig. 3.

The undoped $K_2B_4O_7$ sample (Fig. 3a) exhibits a highly agglomerated morphology composed of irregularly shaped grains with smooth surfaces and loosely packed boundaries. The microstructure suggests that the particles are fused during synthesis, forming dense clusters with a few visible voids. Upon Dy^{3+} incorporation (Fig. 3b), the morphology evolves into a more compact arrangement of fine, plate-like crystallites with an increased degree of aggregation. This morphological refinement can be attributed to the influence of Dy^{3+} ions on the nucleation and growth processes during the thermal treatment stage. The increased ionic field strength of Dy^{3+} compared with K^+ enhances local lattice energy, thereby promoting grain growth control and surface densification.

The corresponding EDS spectra further verify the successful incorporation of Dy^{3+} ions into the host lattice. It should be noted that SEM–EDS is a semi-quantitative technique and the atomic percentages obtained may deviate from the ideal stoichiometric values, particularly

Table 2
Ionic radii (R_m), coordination numbers (CN), and calculated distortion parameters (D_r) for K^+, Dy^{3+}, Li^+ and Na^+ ions in the $K_2B_4O_7$ lattice.

	K		Dy			K		Li			K		Na	
D_r	R_m	CN	R_m	CN	D_r	R_m	CN	R_m	CN	D_r	R_m	CN	R_m	CN
31.98	1.51	8	1.027	8	**39.07**	1.51	8	0.92	8	**21.85**	1.51	8	1.18	8
	Li		**Dy**			**Na**		**Dy**						
D_r	R_m	CN	R_m	CN	D_r	R_m	CN	R_m	*CN*					
10.41	0.92	8	1.027	8	**14.89**	1.18	8	1.027	8					

Table 3
Crystallite size (D) and microstrain (ε) of undoped and doped $K_2B_4O_7$ samples calculated using different line-broadening models (Debye–Scherrer, Monshi–Scherrer, Williamson–Hall, Halder–Wagner, and Size–Strain).

Concentration		$K_2B_4O_7$					
		Undoped	$0.01Dy^{3+}$	$0.03Dy^{3+}$	$0.05Dy^{3+}$	$0.02Dy^{3+}$,$0.03K^{+}$	$0.02Dy^{3+}$,$0.03Na^{+}$
Debye-Scherer	D (nm)	56.48	61.13	63.64	64.62	54.60	59.99
	$\delta \times 10^{-3}$ (nm^{-2})	0.31	0.26	0.24	0.239	0.33	0.27
Monshi-Scherrer	D (nm)	60.31	64.23	71.23	74.45	65.76	70.90
	$\delta \times 10^{-3}$ (nm^{-2})	0.27	0.24	0.19	0.18	0.23	0.19
Williamson-Hall	D (nm)	54.23	64.65	68.96	76.21	56.13	64.36
	$\varepsilon \times 10^{-3}$	2.80	3.44	2.64	2.86	1.43	3.06
Halder-Wagner	D (nm)	60.240	64.10	69.930	72.99	53.19	59.88
	$\varepsilon \times 10^{-3}$	11.3490	12.86	12.6	15.76	9.27	14.06
Size-Strain	D (nm)	58.630	63.23	68.96	72.40	59.59	62.15
	$\varepsilon \times 10^{-3}$	2.3298	2.05	1.9004	1.39	1.80	6.24

for light elements such as boron and oxygen. In the undoped sample, only the characteristic peaks of K, B, and O are detected, consistent with the nominal $K_2B_4O_7$ stoichiometry. In contrast, the Dy^{3+}-doped sample clearly shows additional peaks corresponding to Dy^{3+}, confirming its presence within the material. The quantified elemental data (inset tables of Fig. 3a–b) demonstrate a Dy^{3+} content of approximately 3.36 wt%, which is close to the intended nominal composition. The relative atomic percentages of K, B, and O remain within experimental uncertainty, indicating that Dy^{3+} substitution does not lead to the formation of secondary Dy^{3+}-containing phases, within the semi-quantitative limitations of SEM–EDS analysis. These findings confirm that Dy^{3+} ions are successfully incorporated into the $K_2B_4O_7$ matrix rather than forming secondary Dy-containing phases, in agreement with the XRD results. Furthermore, the microstructural evolution observed upon Dy^{3+} addition suggests improved particle compaction and reduced porosity, features that can be beneficial for enhancing the optical and photoluminescence (PL) performance of the material.

3.3. Vibrational analysis (FTIR and Raman spectroscopy)

The vibrational characteristics of the undoped, Dy^{3+}-doped, and Li^{+}/Na^{+} co-doped $K_2B_4O_7$ phosphors were investigated using Fourier-transform infrared (FTIR) and Raman spectroscopy to evaluate the preservation of the borate network and identify possible structural perturbations induced by the dopant ions. The corresponding spectra are presented in Fig. 4a and c, respectively.

The FTIR spectra of all compositions (Fig. 4a) display the characteristic absorption bands of crystalline potassium tetraborate. The strong absorption at 1283 cm^{-1} is attributed to the asymmetric stretching vibrations of B_3–O bonds in trigonal [BO_3] units, while the prominent band near 987 cm^{-1} corresponds to the symmetric stretching mode of tetrahedral [BO_4] groups [19–21]. The peaks located at 843 cm^{-1} and 729 cm^{-1} originate from the bending vibrations of B–O–B linkages connecting [BO_3] and [BO_4] structural groups. Additional weak bands appearing at 683, 591, 551, and 517 cm^{-1} are associated with bending and deformation modes of the borate network, as well as lattice vibrations involving K–O bonds [21,22].

All Dy^{3+}-doped and Li^{+}/Na^{+} co-doped samples exhibit FTIR features that closely resemble those of the undoped host, confirming that the fundamental borate skeleton remains intact upon doping. Nonetheless, subtle shifts of 1–4 cm^{-1} and mild band broadening are observed, particularly around the [BO_4] stretching region. These variations indicate minor local distortions caused by the substitution of K^{+} (1.51 Å) by Dy^{3+} (1.027 Å) and the incorporation of smaller charge-compensating Li^{+} or Na^{+} ions. Such local modifications are consistent with lattice relaxation and strain minimization, as previously revealed by XRD and microstrain analyses.

To quantitatively evaluate the influence of Dy^{3+} and Na^{+} co-doping on the boron–oxygen coordination environment, Gaussian peak deconvolution was applied to the FTIR spectrum of the representative Dy^{3+}–Na^{+} co-doped $K_2B_4O_7$ sample (See Fig. 4b). The analysis focused on the BO_4 (~987 cm^{-1}) and BO_3 (~1283 cm^{-1}) vibrational bands, from which the full width at half maximum (FWHM) values and integrated peak areas were extracted.

The BO_4-related band exhibits a larger FWHM compared to the BO_3 band, indicating enhanced local structural disorder and distortion around tetrahedral boron units induced by the incorporation of Dy^{3+} ions and charge-compensating Na^{+} ions. Furthermore, the calculated BO_4/BO_3 integrated area ratio confirms a redistribution of boron coordination units upon co-doping, evidencing a partial transformation from trigonal BO_3 units to tetrahedral BO_4 units. These quantitative results demonstrate that Dy^{3+}–Na^{+} co-doping modifies the local borate network structure rather than merely inducing peak position shifts.

The Raman spectra (Fig. 4c) further corroborate the FTIR observations. The undoped $K_2B_4O_7$ sample exhibits distinct vibrational peaks at approximately 237, 349, 397, 459, 495, 573, 752, 932, and 1011 cm^{-1}, in good agreement with the reported vibrational modes of borate lattices [19,20]. Notably, the bands near 525, 760, 915, and 994 cm^{-1} can be attributed to polyborate species, particularly the pentaborate group $B_5O_6(OH)_4^-$, as recently identified by Luo et al. [23].The bands below 500 cm^{-1} correspond to the bending modes of B–O–B linkages and K–O lattice vibrations, whereas those within the 700–1100 cm^{-1} region are attributed to the symmetric and asymmetric stretching of [BO_3] and [BO_4] units. The coexistence of both trigonal and tetrahedral boron coordination confirms the typical mixed borate structure of $K_2B_4O_7$. With increasing Dy^{3+} concentration, the Raman peaks become slightly broader and exhibit minor blue shifts, signifying enhanced B–O bond covalency and local lattice compression due to the higher charge density of Dy^{3+} ions. In the co-doped samples, Li^{+} and Na^{+} ions induce subtle variations in the relative intensity of the [BO_4]-related bands, which may be associated with the stabilization of the borate framework through effective charge compensation and improved structural ordering.

Overall, the FTIR and Raman analyses confirm that Dy^{3+} and Li^{+}/Na^{+} ions are successfully incorporated into the $K_2B_4O_7$ lattice without altering its essential borate structure. The minor frequency shifts and band broadening observed are indicative of localized distortions around the dopant sites rather than any fundamental phase transformation. These findings are in excellent agreement with the XRD, Rietveld, and microstrain analyses, collectively demonstrating that the doped and co-doped $K_2B_4O_7$ phosphors retain high structural stability and crystallinity.

To complement the FTIR results, a quantitative Raman analysis was performed on the representative Dy^{3+}–Na^{+} co-doped $K_2B_4O_7$ sample using Gaussian peak deconvolution (see Fig. 4d). The Raman bands associated with trigonal BO_3 units (boroxol ring vibration, ~758 cm^{-1}) and tetrahedral BO_4 units (~960–970 cm^{-1}) were fitted to extract full width at half maximum (FWHM) values and integrated peak intensities. The BO_4-related Raman mode exhibits both increased intensity and noticeable band broadening compared to the BO_3 mode, resulting in an

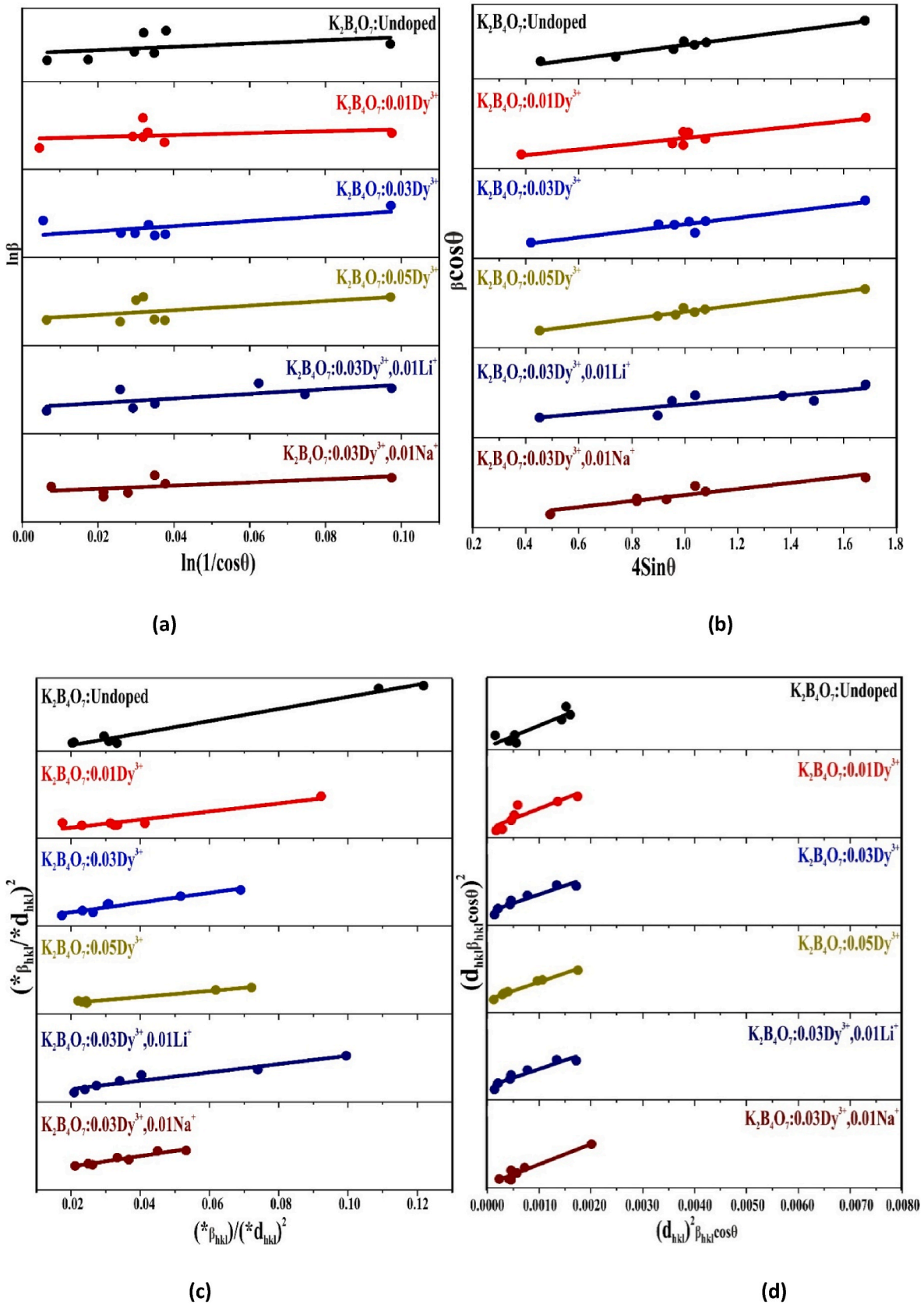

Fig. 2. (a) Monshi–Scherrer, (b) Williamson–Hall, (c) Halder–Wagner, and (d) Size–Strain plots for undoped, Dy^{3+}-doped, and Li^{+}/Na^{+} co-doped $K_2B_4O_7$ samples.

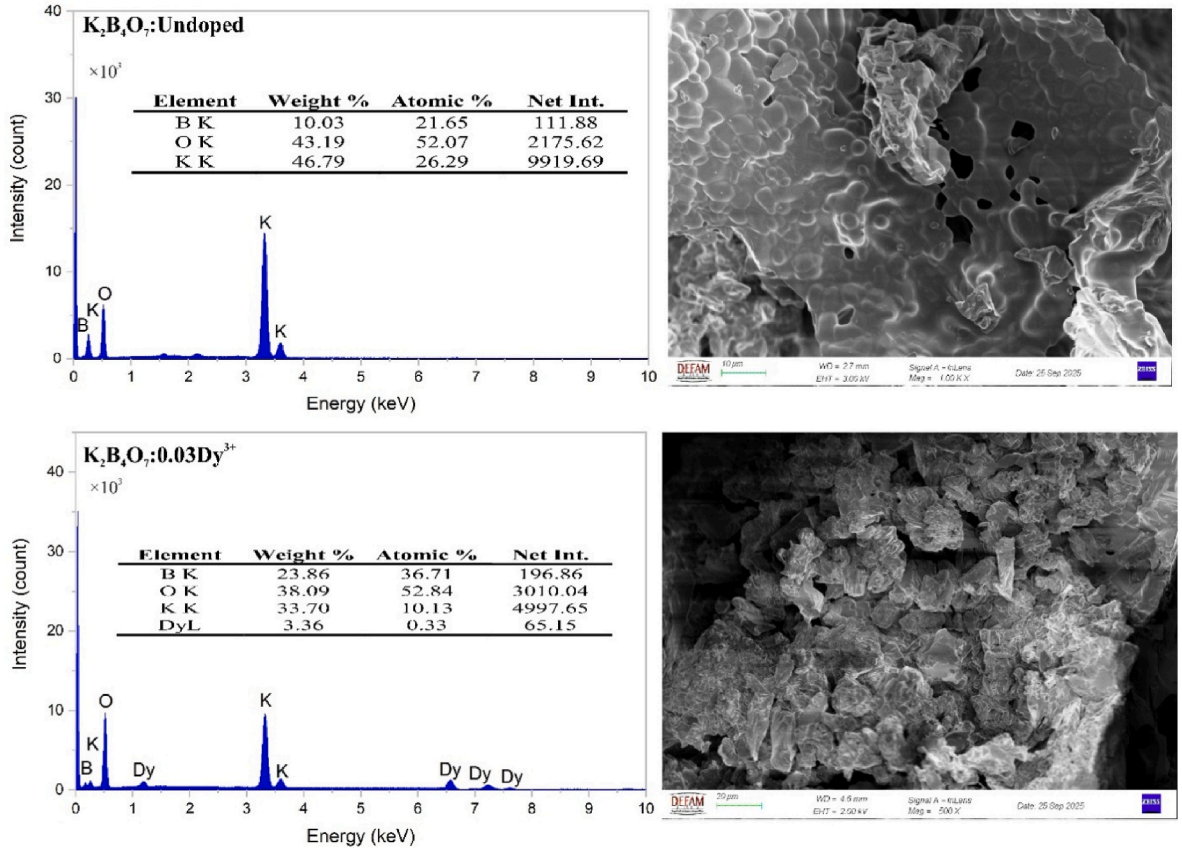

Fig. 3. SEM micrographs and EDS spectra of (a) undoped $K_2B_4O_7$ and (b) $K_2B_4O_7$:0.03Dy^{3+} samples showing morphological evolution and elemental verification of Dy^{3+} incorporation.

enhanced BO_4/BO_3 intensity ratio. This observation indicates a redistribution of boron coordination units toward tetrahedral BO_4 configurations upon Dy^{3+}–Na^+ co-doping. The agreement between Raman-derived intensity ratios and FTIR-based quantitative analysis provides independent confirmation of the modification of the local boron–oxygen coordination environment, rather than a simple peak position shift. It should be emphasized that the larger BO_4/BO_3 ratio obtained from Raman spectroscopy compared to FTIR analysis is expected, as Raman scattering is intrinsically more sensitive to tetrahedral [BO_4] units, whereas FTIR probes both trigonal [BO_3] and tetrahedral [BO_4] units more evenly.

The quantitative parameters extracted from the Gaussian peak fitting of the FTIR and Raman spectra for the representative Dy^{3+}–Na^+ co-doped $K_2B_4O_7$ sample are summarized in Table 4. The table lists the peak positions, full width at half maximum (FWHM), integrated peak areas, and the corresponding BO_4/BO_3 ratios obtained from both spectroscopic techniques. The consistency between FTIR- and Raman-derived BO_4/BO_3 ratios further supports the modification of the local boron–oxygen coordination environment induced by Dy^{3+}–Na^+ co-doping. The Dy^{3+}–Na^+ co-doped composition was selected as a representative sample due to its pronounced vibrational features and clear separation of BO_3 and BO_4 modes, enabling reliable quantitative fitting.

3.4. Photoluminescence characteristics of Dy^{3+}-doped $K_2B_4O_7$ phosphor

The photoluminescence (PL) properties of Dy^{3+}-activated $K_2B_4O_7$ phosphors were examined to understand the optical transitions and local environment of Dy^{3+} ions within the host lattice. Fig. 5a presents the excitation and emission spectra of the representative $K_2B_4O_7$:0.005Dy^{3+} sample, recorded at room temperature.

The excitation spectrum monitored at 575 nm (corresponding to the characteristic yellow emission of Dy^{3+}) displays several sharp bands originating from the intra-$4f^9$ transitions of Dy^{3+} ions from the ground state $^6H_{15/2}$ to higher excited states. The distinct excitation bands observed at 294, 323, 349, 364, and 386 nm correspond to the transitions $^6H_{15/2} \rightarrow {}^4D_{7/2}$, $^6P_{3/2}$, $^6P_{7/2}$, $^6P_{5/2}/{}^4I_{11/2}$, and $^6H_{15/2} \rightarrow {}^4M_{19/2}/{}^4K_{17/2}$, respectively [11,24]. In addition, a broad charge-transfer band (CTB) centered around 233 nm is assigned to the $O^{2-} \rightarrow Dy^{3+}$ charge-transfer transition, indicating strong host–activator coupling [25–27].

Upon excitation at 364 nm, the emission spectrum exhibits three dominant emission peaks located at 482, 576, and 644 nm, which can be assigned to the $^4F_{9/2} \rightarrow {}^6H_{15/2}$ (blue), $^4F_{9/2} \rightarrow {}^6H_{13/2}$ (yellow), and the red emission band at ~644 nm is tentatively assigned to the $^4F_{9/2} \rightarrow {}^6H_{11/2}$ transitions of Dy^{3+} ions, respectively. This emission corresponds to the most intense Stark component of the transition, while weaker features observed near ~670 nm are attributed to other Stark components rather than to a separate emitting center. It is noted that the $^4F_{9/2} \rightarrow {}^6H_{11/2}$ transition of Dy^{3+} ions is often reported at longer wavelengths (~660–680 nm) in many host materials; however, its exact spectral position and relative intensity are strongly host-dependent due to crystal-field-induced Stark splitting and local site symmetry effects. In low-symmetry crystal fields, this transition may split into multiple Stark components distributed over a broad spectral range, with one component occasionally exhibiting higher relative intensity than the others.

Similar host-dependent shifts of the Dy^{3+} $^4F_{9/2} \rightarrow {}^6H_{11/2}$ transition toward the 640–650 nm region have been reported in several oxide- and borate-based hosts, where strong crystal-field effects lead to pronounced Stark splitting [28–30]. A weak near-infrared emission band is also observed at ~758 nm, which is consistent with the typically reported weak near-infrared Dy^{3+} emission originating from the $^4F_{9/2}$ level in crystalline hosts. According to the comprehensive optical spectroscopy

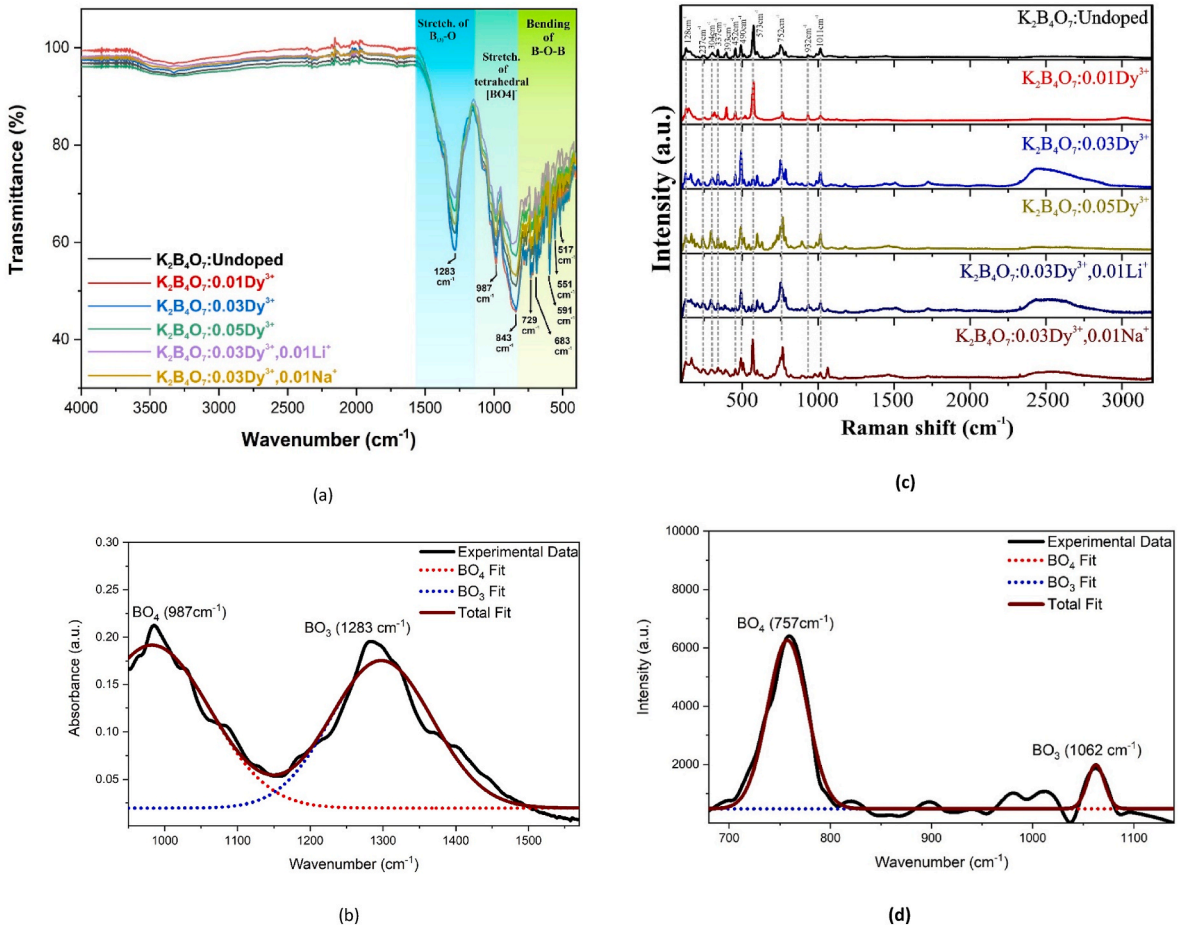

Fig. 4. (a) FTIR spectra of undoped, Dy^{3+}-doped, and Li^{+}/Na^{+} co-doped $K_2B_4O_7$ samples, illustrating the preservation of the borate framework and subtle local distortions induced by Dy^{3+} incorporation and alkali co-doping. (b) Representative deconvoluted FTIR spectrum of the Dy^{3+}–Na^{+} co-doped $K_2B_4O_7$ sample showing the BO_3 (~1283 cm^{-1}) and BO_4 (~987 cm^{-1}) vibrational components obtained by Gaussian peak fitting. (c) Raman spectra of undoped, Dy^{3+}-doped, and Li^{+}/Na^{+} co-doped $K_2B_4O_7$ samples, confirming the coexistence of trigonal [BO_3] and tetrahedral [BO_4] units within the borate lattice. (d) Representative deconvoluted Raman spectrum of the Dy^{3+}–Na^{+} co-doped $K_2B_4O_7$ sample highlighting the BO_3 (boroxol ring, ~758 cm^{-1}) and BO_4 (~960–970 cm^{-1}) vibrational modes.

Table 4
Quantitative FTIR and Raman peak fitting parameters of the representative Dy^{3+}–Na^{+} co-doped $K_2B_4O_7$ sample. In the Raman analysis, the BO_3 band corresponds to the boroxol ring vibration near ~758 cm^{-1}, while the BO_4-related stretching modes appear in the ~900–1100 cm^{-1} region. The BO_4/BO_3 ratios were calculated from the integrated peak areas obtained by Gaussian fitting.

FTIR	Peak Position	FWHM	Peak area	BO_4/BO_3
BO_4 (tetrahedral stretching)	982	186.56	12.37705	0.61
BO_3 (trigonal stretching)	1297	164.55	20.28224	
Raman	**Peak Position**	**FWHM**	**Peak area**	**BO_4/BO_3**
BO_4 (boroxol ring vibration)	757	45.92	331747.92191	6.07
BO_3 (tetrahedral stretching)	1062	20.17	54698.55196	

analysis of Dy^{3+} in crystalline hosts by Cavalli [31], emission from the $^4F_{9/2}$ level is typically dominated by blue (~485 nm) and yellow (~575 nm) bands, accompanied by weaker red and near-infrared components whose spectral position and relative intensity are strongly dependent on the host crystal field and site symmetry. Cavalli further emphasizes that Dy^{3+} emission bands should not be assigned assuming universal fixed peak positions, as crystal-field strength and symmetry can significantly redistribute Stark components over a broad spectral range in different hosts, consistent with the observed red emission around ~644 nm in the present $K_2B_4O_7$-based system. The yellow emission (576 nm) dominates the spectrum, yielding a yellow-to-blue intensity ratio (I_{576}/I_{482}) of 1.87. Such a relatively high ratio indicates that Dy^{3+} ions occupy low-symmetry, non-centrosymmetric sites within the $K_2B_4O_7$ lattice, promoting the electric dipole $^4F_{9/2} \rightarrow {}^6H_{13/2}$ transition over the magnetic dipole $^4F_{9/2} \rightarrow {}^6H_{15/2}$ one [32,33]. Among these excitation lines, the bands centered at 349, 364, and 386 nm exhibit relatively higher intensities compared with the other transitions, indicating that the excitation profile of $K_2B_4O_7$:Dy^{3+} matches well with the emission range of commercial InGaN-based near-UV LED chips (350–410 nm).

The coexistence of the blue and yellow emissions leads to a near-white luminescence, confirming efficient energy transfer from the host to Dy^{3+} ions through the charge-transfer band. This balanced dual emission is characteristic of Dy^{3+}-activated phosphors and is particularly beneficial for white-light-emitting devices and display applications.

Overall, these PL features confirm that Dy^{3+} ions are effectively incorporated into the $K_2B_4O_7$ lattice and that the host matrix provides a suitable environment for radiative 4f–4f transitions with high spectral purity and thermal stability.

To further elucidate the observed excitation and emission behaviour, the schematic energy-level diagram of Dy^{3+} ions in the $K_2B_4O_7$ host matrix is presented in Fig. 5b. The left part of the diagram depicts the

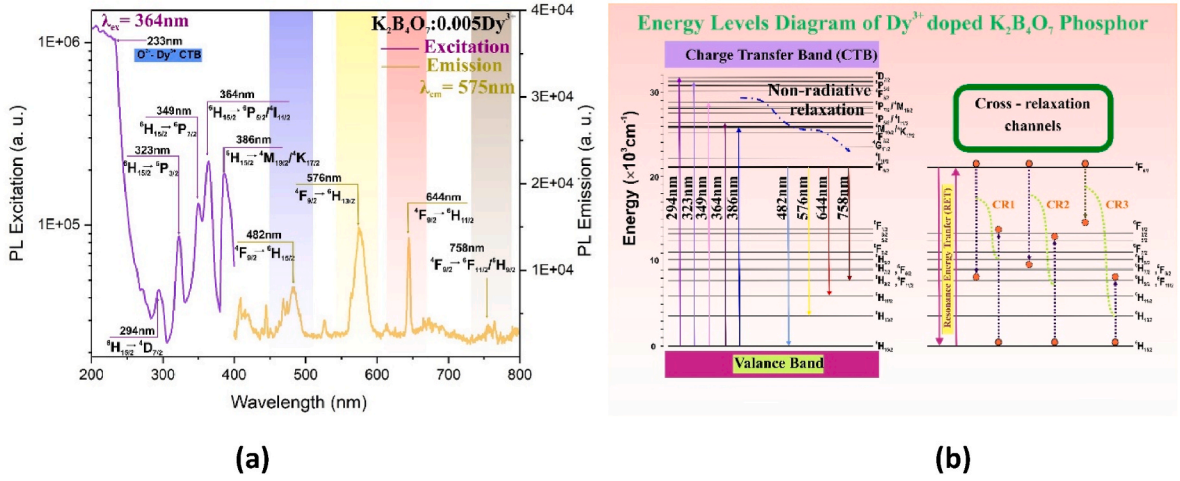

Fig. 5. (a) Excitation (λ_{em} = 575 nm) and emission (λ_{ex} = 364 nm) spectra of $K_2B_4O_7$:0.005Dy^{3+} phosphor recorded at room temperature (b) Schematic energy-level diagram of Dy^{3+} ions in the $K_2B_4O_7$ phosphor, illustrating excitation bands, non-radiative relaxations, radiative transitions, and cross-relaxation (CR_1–CR_3) channels responsible for the observed blue, yellow, and red emissions. (For interpretation of the references to color in this figure legend, the reader is referred to the Web version of this article.)

characteristic intra-4f transitions responsible for the excitation bands, while the broad charge-transfer band (CTB) near 233 nm corresponds to the $O^{2-} \rightarrow Dy^{3+}$ electron transfer process. Upon excitation through either the CTB or near-UV f–f transitions, excited Dy^{3+} ions are promoted to higher multiplets, followed by stepwise non-radiative relaxations to the metastable $^4F_{9/2}$ level. Radiative transitions from this level produce the characteristic emissions at 482, 576, and 644 nm, consistent with the spectral features shown in Fig. 5.

The right section of the diagram illustrates the cross-relaxation (CR) channels that occur between adjacent Dy^{3+} ions, namely CR_1: ($^4F_{9/2}$, $^6H_{15/2}$) → ($^6F_{3/2}$, $^6F_{9/2}$), CR_2: ($^4F_{9/2}$, $^6H_{13/2}$) → ($^6F_{7/2}$, $^6H_{11/2}$), and CR_3: ($^4F_{9/2}$, $^6H_{11/2}$) → ($^6H_{13/2}$, $^6H_{9/2}$). These resonant energy-transfer pathways facilitate partial depopulation of the $^4F_{9/2}$ level, redistributing excitation energy among neighboring Dy^{3+} centers. At moderate dopant concentrations, such processes enhance the yellow-emitting $^4F_{9/2} \rightarrow {}^6H_{13/2}$ transition while slightly suppressing the blue $^4F_{9/2} \rightarrow {}^6H_{15/2}$ transition, leading to an increased I_{576}/I_{482} ratio and a warm-white luminescence output. However, excessive Dy^{3+} concentration may intensify cross-relaxation to the extent that non-radiative energy migration and quenching centers dominate, reducing overall emission intensity.

The proposed energy-transfer scheme confirms that $K_2B_4O_7$ provides a favorable crystal-field environment for Dy^{3+} ions, supporting efficient host-to-activator transfer through the CTB, balanced blue–yellow emissions, and controllable color tuning via concentration-dependent cross-relaxation dynamics. These mechanisms collectively validate the strong correlation between the experimental PL spectra and the energy-level structure of Dy^{3+} in the $K_2B_4O_7$ matrix.

3.4.1. *Concentration-dependent emission behavior*

The photoluminescence (PL) characteristics of $K_2B_4O_7$:xDy^{3+} phosphors exhibit a pronounced dependence on activator concentration, reflecting the interplay between radiative recombination efficiency, Dy^{3+}–Dy^{3+} interactions, and defect-mediated non-radiative processes. Fig. 6a presents the normalized PL emission spectra of $K_2B_4O_7$:$x$$Dy^{3+}$ (x = 0.005–0.07) under 364 nm excitation, where all samples display the characteristic $^4F_{9/2} \rightarrow {}^6H_{15/2}$ (blue) and $^4F_{9/2} \rightarrow {}^6H_{13/2}$ (yellow) transitions of Dy^{3+}, confirming efficient 4f–4f excitation. Normalization highlights the evolution of spectral shape with concentration, while the variation in overall emission strength is more clearly illustrated **in** Fig. 6 (b).

The normalized integrated PL intensity plotted as a function of Dy^{3+} concentration (Fig. 6b) shows a characteristic rise-and-fall trend typical of rare-earth-doped systems. As the Dy^{3+} content increases from x = 0.005 to 0.03, the emission intensity increases steadily, reaching a maximum at x = 0.03. This enhancement is attributed to improved energy transfer efficiency and a strengthened crystal-field environment around Dy^{3+} ions, which promotes radiative recombination while suppressing defect-related non-radiative pathways. The increase in Dy^{3+} concentration up to this level likely reduces borate-network imperfections and oxygen vacancies, thereby enhancing luminescent efficiency.

Beyond the optimum concentration ($x > 0.03$), the PL intensity declines, indicating the onset of concentration quenching. This quenching arises from cross-relaxation processes and excitation-energy migration among closely spaced Dy^{3+} ions, which increases the probability for energy transfer toward quenching centers rather than radiative emission. The collective behavior demonstrates that 3 wt% Dy^{3+} represents the optimal activator concentration for maximizing luminescence in the $K_2B_4O_7$ host lattice.

To gain deeper insight into the mechanism responsible for the decline in emission intensity at higher Dy^{3+} concentrations, the concentration-quenching behavior was further examined by analysing the spatial distribution and interaction strength of Dy^{3+} ions within the $K_2B_4O_7$ lattice. As the distance between neighboring activator ions decreases beyond the optimum level, non-radiative energy transfer becomes increasingly probable, enabling excitation energy to migrate toward quenching sites instead of contributing to radiative 4f–4f transitions. Evaluating the critical Dy^{3+}–Dy^{3+} separation and the nature of the dominant multipolar interactions therefore provides a quantitative basis for understanding the observed emission trends and the onset of quenching in this system.

To quantitatively clarify the interaction mechanism governing this quenching behavior, the critical distance (R_c) between Dy^{3+} ions was estimated using the Blasse equation, which provides a practical criterion for identifying the type of interaction responsible for non-radiative energy transfer:

Using the Blasse relation,

$$R_c \approx 2\left[\frac{3V}{4\pi x_c N}\right]^{1/3} \tag{3}$$

where V is the unit-cell volume, x_c is the critical Dy^{3+} concentration corresponding to the maximum emission intensity, and N is the number of formula units per unit cell, the critical distance was calculated. Taking $V \approx 622.6$ Å^3, $x_c = 0.03$, and $N = 4$ for the orthorhombic $K_2B_4O_7$ lattice, the estimated value of the critical distance is 10.1 Å. Since this distance

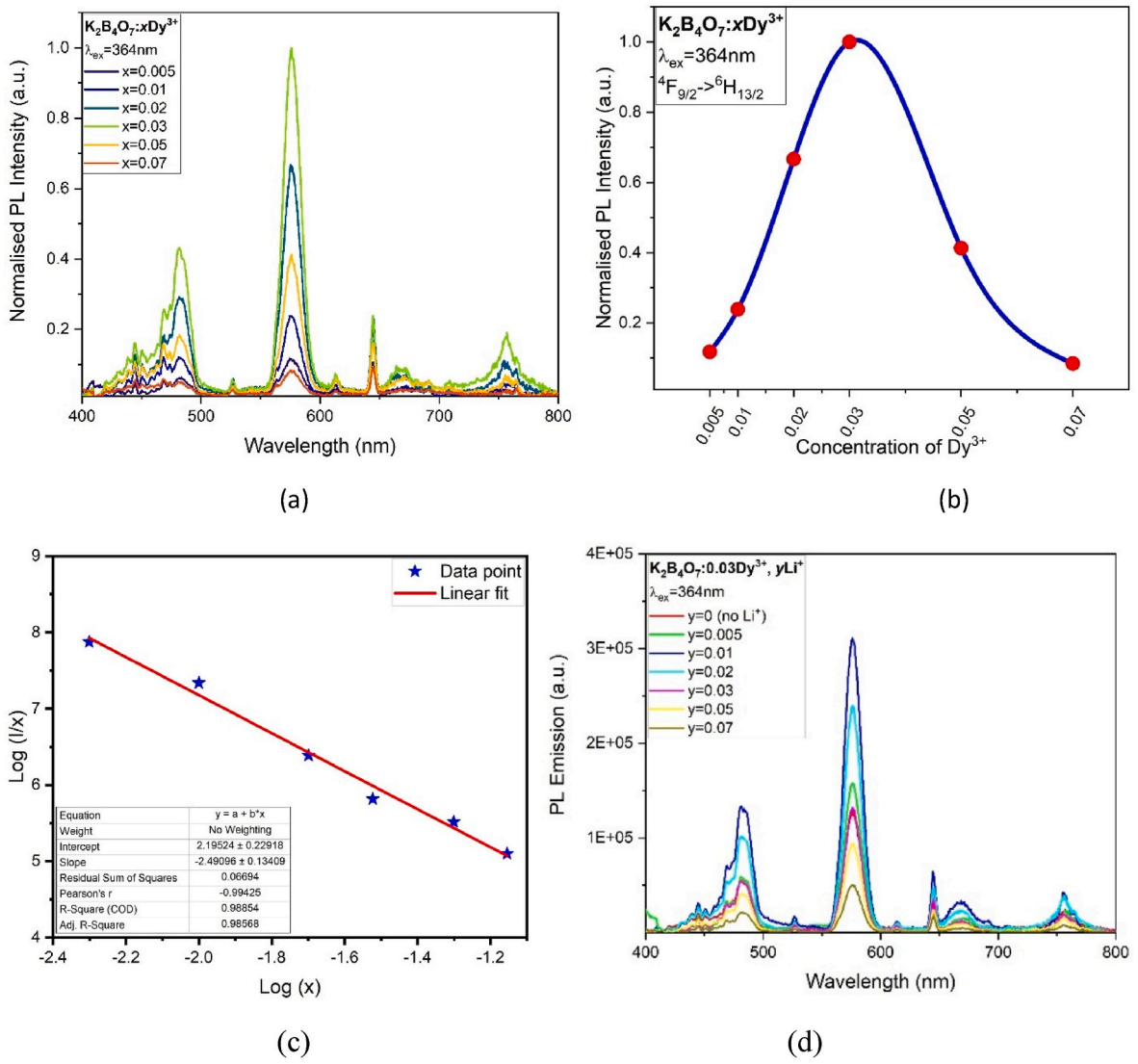

Fig. 6. (a) Room-temperature photoluminescence (PL) emission spectra of $K_2B_4O_7$:xDy^{3+} phosphors (x = 0.005–0.07) under 364 nm excitation (b) Log–log plot of log(I/x) versus log(x) fitted using the Dexter–Van Uitert model to identify the dominant multipolar interaction responsible for concentration quenching. (d) Variation in photoluminescence intensity of $K_2B_4O_7$:0.03Dy^{3+} phosphors with different Li $^+$ doping concentrations.

is significantly larger than the 5 Å threshold typically associated with exchange interactions, it indicates that exchange coupling is not responsible for the observed concentration quenching [34]. Instead, the non-radiative energy transfer must arise from long-range multipolar interactions among Dy^{3+} ions. This observation is consistent with established guidelines in the literature that differentiate exchange-driven processes from multipolar energy-transfer interactions [33,35].

To identify the dominant multipolar mechanism, the emission intensity was analyzed using the Dexter–Van Uitert model [36,37], which predicts the following relationship:

$$\frac{I}{x} = \propto x^{-Q/3} \tag{4}$$

where Q characterizes the type of multipolar interaction. The logarithmic plot of log (I/x) versus log (x) yielded a linear dependence with a slope of −2.49 as shown in Fig. 6c. This corresponds to a multipolar interaction parameter of $Q \approx 7.5$, which lies closest to the theoretical value of Q = 8 associated with dipole–quadrupole interactions. This finding indicates that, beyond the optimal Dy^{3+} concentration, non-radiative energy migration in $K_2B_4O_7$:Dy^{3+} is primarily facilitated through dipole–quadrupole coupling rather than dipole–dipole or exchange-driven processes. Such behavior aligns with established criteria distinguishing between different long-range multipolar energy-transfer pathways in rare-earth-activated borate hosts [38].

The photoluminescence (PL) emission spectra of $K_2B_4O_7$:0.03Dy^{3+} phosphors with varying Li $^+$ content (y = 0–0.07) as shown in Fig. 6d reveal a pronounced dependence of emission intensity on the doping concentration. A significant enhancement in PL intensity is observed up to a Li $^+$ doping level of y = 0.01, beyond which the intensity gradually declines. This enhancement at low doping levels can be attributed to improved crystallinity and the reduction of non-radiative defect centers, as Li^+ ions—due to their small ionic radius and high mobility—effectively occupy interstitial sites and passivate quenching centers [17]. Furthermore, the incorporation of Li $^+$ ions facilitates energy transfer by modifying the local field around Dy^{3+} ions, thereby increasing the radiative recombination probability. However, at higher concentrations (y > 0.01), the excessive Li^+ content disrupts the crystal lattice, leading to the formation of structural distortions and non-radiative recombination centers, which in turn suppress the emission intensity. This concentration quenching behavior is characteristic of rare-earth-doped phosphors and indicates that y = 0.01 represents the

optimal Li^+ doping level for maximizing luminescent efficiency in this host matrix [39–42].

3.4.2. Temperature-dependent PL behavior and thermal stability

The thermal evolution of the photoluminescence properties of $K_2B_4O_7$:0.03Dy^{3+} and Li^+ co-doped $K_2B_4O_7$:0.03Dy^{3+} phosphors was investigated in the temperature range of 300–550 K to evaluate their thermal stability and determine the influence of charge-compensating dopants on the stability of Dy^{3+} emission centers. The 3D temperature-dependent PL maps for $K_2B_4O_7$:0.03Dy^{3+} and $K_2B_4O_7$:0.03Dy^{3+},0.01Li^+ are presented in Fig. 7(a) and (c), respectively, while the corresponding normalized PL intensity variations are shown in Fig. 7(b) and (d).

As seen in Fig. 7a, the Dy^{3+}-activated host exhibits a strong decrease in PL intensity with increasing temperature from 300 K to 450 K. The normalized intensity curve in Fig. 7c shows that the emission at 642 nm decreases to approximately 15 % of its room-temperature value at 450 K, indicating pronounced thermal quenching. This behavior can be attributed to thermally activated non-radiative relaxation processes, where elevated temperatures promote phonon-assisted de-excitation from the $^4F_{9/2}$ level to the ground multiplets of Dy^{3+}. Additionally, higher temperatures enhance cross-relaxation interactions among Dy^{3+} ions, providing extra non-radiative decay channels. Such processes reduce radiative recombination efficiency and lead to the observed suppression of PL intensity.

Interestingly, above 450 K the emission intensity begins to recover, approaching its initial room-temperature value at 550 K. Such a thermal recovery behavior is commonly attributed to the thermally assisted release of carriers from shallow defect states, which subsequently repopulate the excited $^5D_4$ level and enhance radiative emission. These defect states—possibly associated with oxygen-related vacancies inherent to borate lattices—can act as temporary charge reservoirs that become active at elevated temperatures. Similar thermally stimulated detrapping effects have been widely reported in rare-earth-doped borate phosphors and are consistent with the partial anti-thermal quenching observed here.

In contrast, the Li^+ co-doped phosphor exhibits markedly improved thermal behavior. As shown in Fig. 7b, the emission intensity does not decrease significantly with increasing temperature; instead, a gradual and nearly monotonic enhancement is observed up to 550 K. The normalized PL plot in Fig. 7d clearly demonstrates this enhancement, with the 642 nm emission increasing steadily from 300 K to 550 K. This unusual anti-quenching behavior indicates that Li^+ co-doping effectively stabilizes Dy^{3+} emission centers against temperature-induced

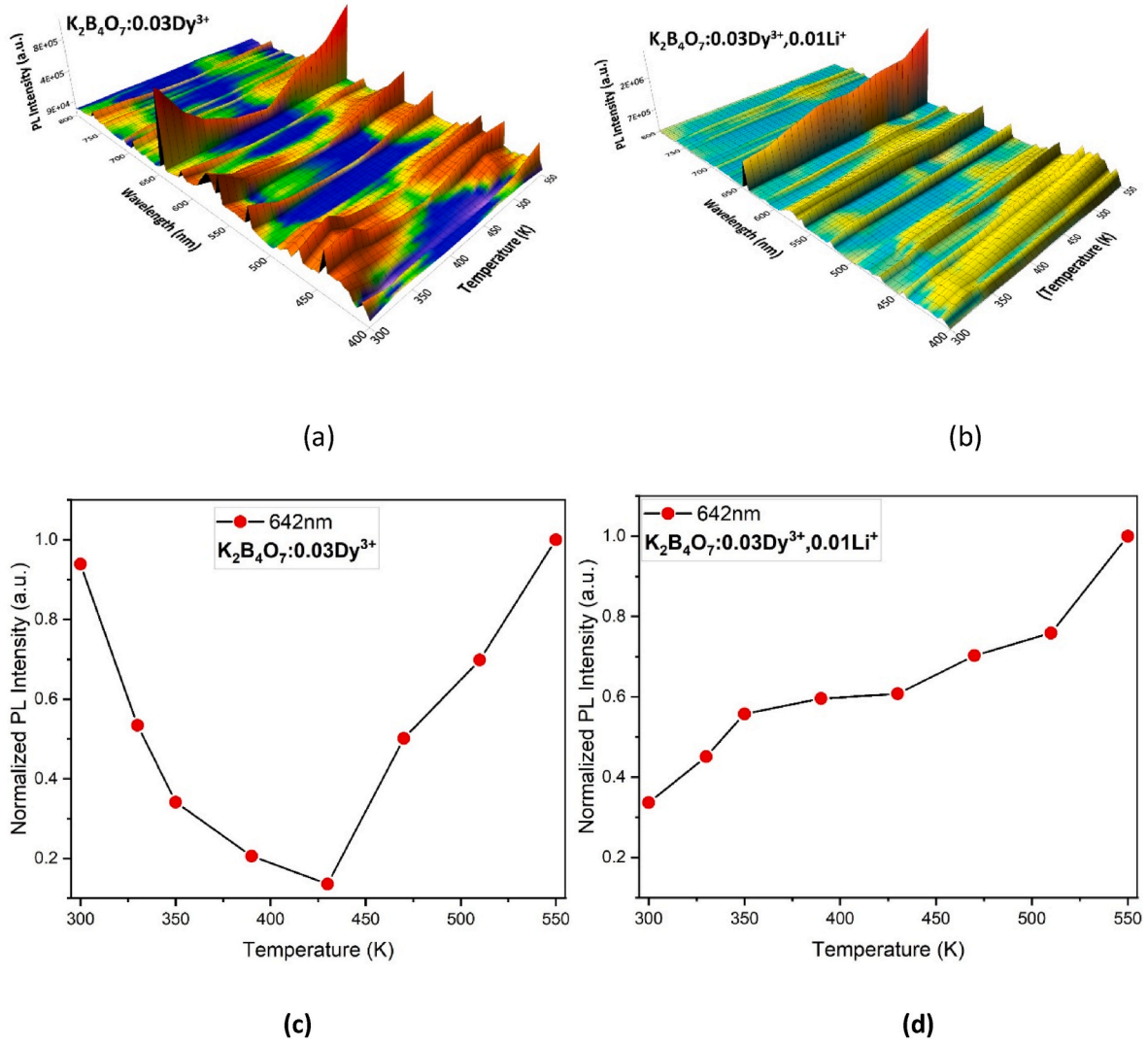

Fig. 7. (a) Temperature-dependent 3D photoluminescence (PL) emission map of $K_2B_4O_7$:0.03Dy^{3+} recorded between 300 and 550 K (b) Corresponding normalized PL intensity variation at 642 nm for $K_2B_4O_7$:0.03Dy^{3+}(c) Temperature-dependent 3D PL emission map of Li^+ co-doped $K_2B_4O_7$:0.03Dy^{3+},0.01Li^+(d) Normalized PL intensity at 642 nm for the Li^+ co-doped sample.

non-radiative losses.

This unusual anti-quenching behavior indicates that Li^+ co-doping effectively stabilizes Dy^{3+} emission centers against temperature-induced non-radiative losses [40,41]. The enhancement in luminescence with increasing temperature arises from several interconnected mechanisms. The incorporation of Li^+ ions modifies the local coordination environment around Dy^{3+} by improving crystal-field symmetry and reducing lattice strain, which strengthens Dy–O bonding and suppresses temperature-activated multipolar non-radiative transfer. At the same time, Li^+ acts as an efficient charge compensator for $Dy^{3+}\rightarrow K^+$ substitution, thereby reducing the density of K^+ vacancies that typically function as non-radiative defect centers. This defect suppression leads to a cleaner local electronic environment, allowing a greater fraction of excited Dy^{3+} ions to undergo radiative 4f–4f transitions. Additionally, the Li^+-modified lattice appears to facilitate the formation of shallow traps that release carriers upon heating; thermally assisted detrapping of these carriers contributes to the observed increase in emission intensity, a behavior often described as thermo-activated photoluminescence. Li^+ co-doping also weakens the dipole–quadrupole interactions identified earlier as the dominant quenching pathway ($Q \approx 7.5$), effectively increasing the Dy^{3+}–Dy^{3+} separation and diminishing the strength of long-range multipolar energy migration. As a result, the Li^+-co-doped sample exhibits markedly superior thermal stability compared to the singly doped counterpart, underscoring its potential for high-temperature or high-power solid-state lighting applications.

The contrasting thermal responses of the two systems highlight the crucial role of charge-compensating ions in regulating the thermal robustness of Dy^{3+} emission. Whereas the undoped $K_2B_4O_7$:Dy^{3+} sample undergoes significant thermal quenching due to phonon-assisted non-radiative relaxation and strong Dy–Dy interactions, Li^+ co-doping introduces structural and electronic modifications that stabilize the $^4F_{9/2}$ excited state, weaken multipolar non-radiative transfer, reduce defect-mediated quenching pathways, and promote thermally activated radiative recombination. Taken together, these effects demonstrate that Li^+ co-doping is an effective strategy for engineering a thermally resilient borate host lattice, thereby enhancing the suitability of $K_2B_4O_7$-based materials for practical photonic applications operating under elevated temperatures. It should be noted that the thermal behavior discussed in this study is based on steady-state photoluminescence (PL) measurements conducted under continuous excitation conditions, which are fundamentally distinct from thermoluminescence (TL) techniques. TL measurements are widely used to probe trap distributions and charge carrier dynamics following thermal stimulation after the removal of excitation, particularly in persistent and afterglow phosphors. In contrast, the anti-thermal-quenching behavior reported here arises from thermally assisted radiative recombination and carrier detrapping that occur simultaneously with excitation. This distinction is critical, as the mechanisms underlying anti-thermal-quenching are more accurately captured through temperature-dependent PL intensity mapping, lifetime analysis, and Arrhenius modeling, all of which are employed in the present work. Therefore, while TL measurements could offer valuable complementary insights into deep trap distributions, the present study emphasizes temperature-dependent PL as the most appropriate technique to directly probe anti-thermal-quenching behavior under continuous excitation. This methodological focus ensures that the observed thermal response is directly aligned with real-time excitation conditions relevant to solid-state lighting applications. Moreover, this approach is consistent with previously reported strategies for evaluating anti-thermal-quenching phenomena in rare-earth-doped phosphors using steady-state photoluminescence techniques.

To quantitatively evaluate the thermal stability of the Dy^{3+} emission, the activation energy (E_a) associated with thermal quenching was determined using the Arrhenius-type relation:

$$ln\left[\left(\frac{I_0}{I}-1\right)\right]=\frac{E_a}{kT}+C \tag{5}$$

The linear fitting of the $ln[(I_0/I-1)]$ versus $1/kT$ plot (Fig. 8) yields a slope of −0.209, corresponding to an activation energy of $E_a \approx 0.21$ eV. The thermal activation energy obtained for $K_2B_4O_7$:Dy^{3+} ($E_a \approx 0.21$ eV) signifies a relatively strong resistance against thermally induced non-radiative relaxation. When compared with previously reported Dy^{3+}-activated phosphor systems, this value positions the present material among the more thermally robust hosts. For instance, $Ca_{19}Zn_2(PO_4)_{14}$:Dy^{3+} exhibits an activation energy of 0.15852 eV [43], $Ca_9LiGd_2/_3(PO_4)_7$:Dy^{3+} shows an even lower value of 0.098 eV [44], while Ca_3TeO_6:Dy^{3+} (0.20 eV) [45] and $NaCaTiTaO_6$:Dy^{3+} (0.18 eV) [46] display moderate thermal barriers. Additionally, Dy^{3+}-doped $LaMgB_5O_{10}$—reported by Hakami et al. [47], exhibits an activation energy of approximately 0.1975 eV, further confirming that borate-based hosts can support relatively high thermal-quenching barriers for Dy^{3+} emission. In this context, the extracted $E_a \approx 0.21$ eV for $K_2B_4O_7$:Dy^{3+} is comparable to or higher than many established Dy^{3+} systems, highlighting the inherently rigid and low-phonon tetraborate framework that effectively suppresses thermally activated non-radiative pathways. These comparisons demonstrate that $K_2B_4O_7$:Dy^{3+} is a promising thermally stable yellow-emitting phosphor, suitable for high-temperature or high-power photonic applications.

3.4.3. *Decay dynamics and lifetime analysis of Dy^{3+} emission*

The decay behavior of the Dy^{3+} emission was investigated to elucidate the recombination dynamics and evaluate the influence of activator concentration and alkali-ion co-doping on non-radiative relaxation pathways. Fig. 9 shows the luminescence decay curves for $K_2B_4O_7$:xDy^{3+} with different Dy^{3+} concentrations ($x = 0.01, 0.03, 0.05$), together with the $0.03Dy^{3+}$ samples co-doped with Li^+ and Na^+ ions.

All decay profiles exhibit non-single-exponential behavior, which is typical for Dy^{3+} in low-phonon-energy borate hosts due to the presence of multiple local environments and energy migration among Dy^{3+} ions. Consequently, the decay curves were fitted using a biexponential model:

$$I(t)=A_1e^{-t/\tau_1}+A_2e^{-t/\tau_2} \tag{6}$$

and the average lifetime was calculated using:

$$\tau_{avg}=\frac{\sum A_i\tau_i^2}{\sum A_i\tau_i} \tag{7}$$

For the singly doped compositions, the average lifetime decreases with increasing Dy^{3+} concentration. The $K_2B_4O_7$:$0.01Dy^{3+}$ sample

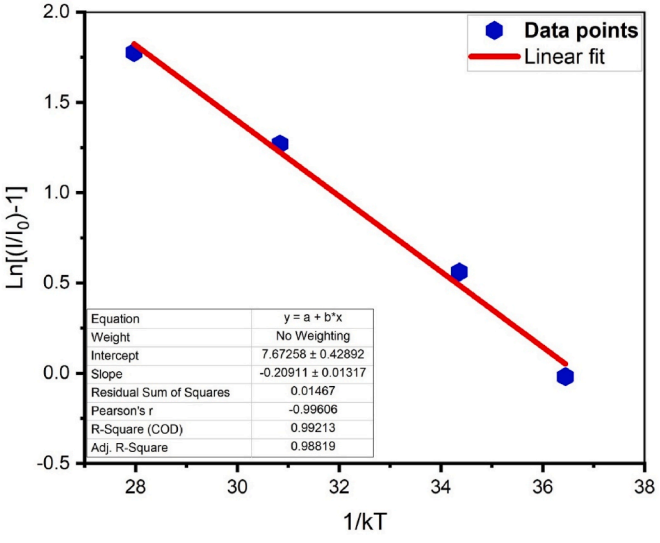

Fig. 8. Arrhenius plot of $Ln[(I/I_0)^{-1}]$ versus 1/kT for the $K_2B_4O_7$:Dy^{3+} phosphor, showing the linear fitting used to extract the thermal quenching activation energy.

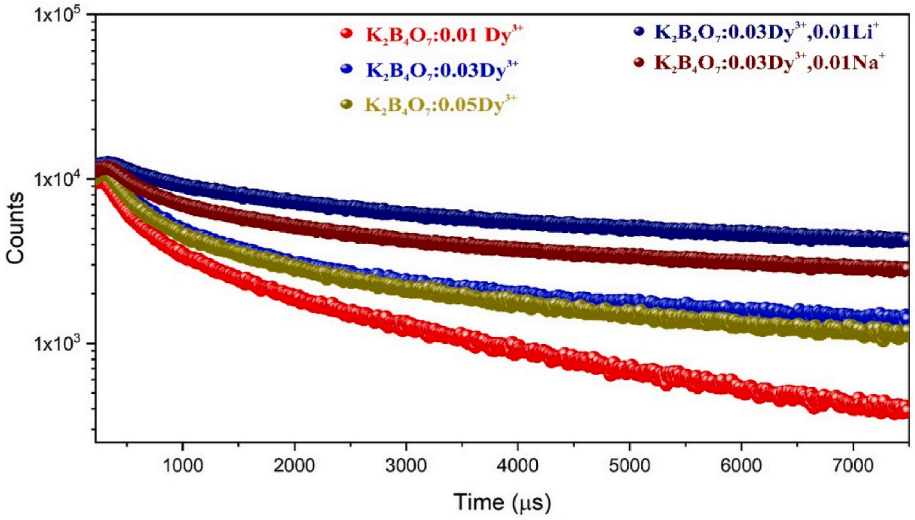

Fig. 9. Luminescence decay curves of $K_2B_4O_7$:xDy^{3+} phosphors with different Dy^{3+} concentrations (x = 0.01, 0.03, 0.05) and co-doped compositions (0.03Dy^{3+} + 0.01Li^+ and 0.03Dy^{3+} + 0.01Na^+), monitored at the $^4F_{9/2} \rightarrow {}^6H_{13/2}$ transition.

exhibits the longest τ_{avg}, whereas higher Dy^{3+} loadings (0.05Dy^{3+}) result in shorter decay times due to enhanced cross-relaxation and multipolar energy migration effects among closely spaced Dy^{3+} ions. These processes accelerate non-radiative de-excitation from the $^4F_{9/2}$ level, leading to reduced lifetimes.

The fitted parameters summarized in Table 5 clearly show that Li^+ co-doping significantly enhances τ_{avg}, increasing the lifetime from 1589 μs (undoped 0.03Dy^{3+}) to 2517 μs. This substantial improvement confirms that Li^+ effectively reduces defect-mediated quenching and suppresses Dy^{3+}–Dy^{3+} energy migration by providing efficient charge compensation and lowering lattice strain around Dy^{3+} ions. Na^+ co-doping also leads to a moderate increase in τ_{avg}, although the effect is less pronounced, consistent with its comparatively weaker ability to compensate for local charge imbalance.

These results reinforce the PL intensity and thermal-quenching trends discussed earlier, demonstrating that Li^+ co-doping stabilizes the $^4F_{9/2}$ state of Dy^{3+}, mitigates non-radiative decay, and enhances the overall emission efficiency of the $K_2B_4O_7$ host. The combined spectroscopic evidence confirms the beneficial role of alkali co-dopants—particularly Li^+—in optimizing the optical performance of borate-based Dy^{3+} phosphors.

These observations support the conclusions drawn from the PL intensity and thermal-quenching analyses: Li^+ co-doping effectively passivates quenching centers, reduces Dy–Dy interaction probability, and stabilizes the $^4F_{9/2}$ excited state. Consequently, the lifetime enhancement corroborates the beneficial role of Li^+ as an efficient charge compensator in $K_2B_4O_7$-based Dy^{3+} phosphors.

Table 5
Biexponential decay fitting parameters (τ_1, τ_2), their relative amplitude contributions, average lifetimes (τ_{avg}), and goodness-of-fit values (χ^2) for $K_2B_4O_7$:$x$$Dy^{3+}$ phosphors with varying Dy^{3+} concentrations and Li^+/Na^+ co-doping.

		Time(μs)	Rel.%	τ_{avg}(μs)	χ^2
$K_2B_4O_7$:0.01Dy^{3+}	τ_1	24.280	20.05	1644.994	1.2115
	τ_2	1685.650	79.95		
$K_2B_4O_7$:0.03Dy^{3+}	τ_1	25.796	20.25	1589.386	1.3737
	τ_2	1629.063	79.75		
$K_2B_4O_7$:0.05Dy^{3+}	τ_1	25.192	18.91	1707.946	1.3965
	τ_2	1747.202	81.09		
$K_2B_4O_7$:0.03Dy^{3+},0.01Li^+	τ_1	39.276	7.75	2516.846	1.2927
	τ_2	2537.657	92.25		
$K_2B_4O_7$:0.03Dy^{3+},0.01Na^+	τ_1	19.604	4.65	1306.986	1.1475
	τ_2	1317.600	95.35		

3.5. Judd–Ofelt analysis of Dy^{3+} ions in $K_2B_4O_7$ and Li^+-Codoped $K_2B_4O_7$ phosphors

This section presents a comprehensive Judd–Ofelt analysis of Dy^{3+} ions in $K_2B_4O_7$ in order to quantify the electric-dipole transition strengths, radiative probabilities, and the influence of Li^+ co-doping on the local ligand environment. The Judd–Ofelt formalism provides a rigorous framework for evaluating electric-dipole activity, radiative decay pathways, and intrinsic emission efficiency, thereby enabling a deeper understanding of the $^4F_{9/2}$ emission behavior observed in the synthesized phosphors.

According to Judd–Ofelt theory, the electric-dipole line strength of a transition from an initial state $|\psi_J\rangle$ to a final state $|\psi_{J'}\rangle$ is expressed as: $S_{ED}(J \rightarrow J') = \sum_{\lambda=2,4,6} \Omega_\lambda \left|\langle \Psi J || U^{(\lambda)} || \Psi' J' \rangle\right|^2$ where Ω_2, Ω_4 and Ω_6 are the Judd–Ofelt intensity parameters, and $\langle \Psi J || U^{(\lambda)} || \Psi' J' \rangle$ are the doubly-reduced matrix elements of the unit-tensor operators for Dy^{3+}.

The spontaneous radiative transition rate for 4f–4f transitions is given by:

$$A_{J \rightarrow J'} = \frac{64\pi^4 e^2}{3h(2J+1)\lambda^3} \chi S_{ED}(J \rightarrow J') + A_{MD} \quad (8)$$

where λ is the transition wavelength and A_{MD} is the magnetic-dipole contribution. The local-field correction factor χ is:

$$\chi = \frac{n(n^2+2)^2}{9} \quad (9)$$

In this study, the refractive index of $K_2B_4O_7$ was taken as n = 1.47. The total radiative decay probability and radiative lifetime of the $^4F_{9/2}$ level are:

$$A_{tot} = \sum_{J'} A_{J \rightarrow J'} \quad (10)$$

$$\tau_{rad} = \frac{1}{A_{tot}} \quad (11)$$

The branching ratio for an individual transition is:

$$\beta_{J \rightarrow J'} = \frac{A_{J \rightarrow J'}}{A_{tot}} \quad (12)$$

The internal quantum efficiency is:

$$\eta = \frac{\tau_{exp}}{\tau_{rad}} \quad (13)$$

The integrated emission intensities of the 482, 576, 644, and 758 nm transitions were used to determine the relative line strengths of the Dy^{3+} $^4F_{9/2} \rightarrow {}^6H_J$ and ^6F_J emission channels. The normalized values, together with the corresponding branching ratios β, are presented in Table 6. These parameters provide a consistent representation of how each radiative pathway contributes to the overall de-excitation of the $^4F_{9/2}$ level.

As shown in Table 6(a), the undoped $K_2B_4O_7$:0.03Dy^{3+} sample displays its strongest contribution from the yellow $^4F_{9/2} \rightarrow {}^6H_{13/2}$ transition, accounting for more than half of the total emission intensity ($\beta = 0.553$). A similar trend is observed in Table 6(b) for the Li^+-codoped sample, where this transition remains dominant ($\beta = 0.548$), confirming its electric-dipole character and sensitivity to local lattice asymmetry.

The slight enhancement in the $^4F_{9/2} \rightarrow {}^6H_{15/2}$ blue transition observed for the Li^+-codoped phosphor ($\beta = 0.317$) further suggests that charge compensation modifies the Dy–O coordination environment, influencing the distribution of radiative probabilities among the emission channels.

The yellow emission band corresponding to $^4F_{9/2} \rightarrow {}^6H_{13/2}$ exhibits the highest β value in both compositions, confirming its strong electric-dipole character and the placement of Dy^{3+} at non-centrosymmetric sites. Notably, Li^+ co-doping slightly enhances this transition's branching ratio, signaling a more asymmetric Dy^{3+}–O^{2-} environment.

The experimental line strengths and the standard reduced matrix elements of the Dy^{3+} 4f–4f transitions were used to determine the Judd–Ofelt parameters through a least-squares fitting procedure. As summarized in Table 7, the extracted Ω_2, Ω_4, and Ω_6 values provide quantitative insight into the degree of asymmetry, covalency, and structural rigidity of the Dy–O coordination environment. The notable increase in Ω_2 upon Li^+ co-doping reflects an enhancement in local lattice distortion and Dy–O bond polarizability, while the moderate increases in Ω_4 and Ω_6 are consistent with strengthened electric-dipole contributions within the $^4F_{9/2}$ manifold.

The Ω_2 parameter displays a noticeable increase upon Li^+ co-doping, signifying enhanced asymmetry and Dy–O bond polarizability. Similarly, the moderate increases in Ω_4 and Ω_6 reflect a strengthening of the electric-dipole mechanism and a reduction in multiphonon relaxation probabilities.

The radiative probabilities obtained from the Judd–Ofelt analysis were used to estimate the radiative lifetime of the $^4F_{9/2}$ emitting level. As presented in Table 8, the comparison between the calculated radiative lifetimes (τ_{rad}) and the experimentally measured decay times (τ_{avg}) allows a reliable determination of the internal quantum efficiency (η). The Li^+-codoped sample exhibits a markedly longer τ_{avg} and a higher η value, indicating a significant reduction in non-radiative relaxation pathways and an overall enhancement of the Dy^{3+} emission performance.

The combined Judd–Ofelt results clearly demonstrate that Dy^{3+} ions occupy non-centrosymmetric coordination sites within the $K_2B_4O_7$ lattice, enabling strong electric-dipole transitions dominated by the hypersensitive $^4F_{9/2} \rightarrow {}^6H_{13/2}$emission. Li^+ co-doping further amplifies this asymmetry, as reflected by the systematic increase in Ω_2, Ω_4, and Ω_6, together with the substantial enhancement in both radiative lifetime and internal quantum efficiency. These improvements confirm that Li^+ effectively modifies the Dy–O ligand field, suppressing non-radiative relaxation channels and strengthening electric-dipole activity. Overall, the near-unity quantum yield and intensified hypersensitive transitions highlight the potential of Li^+-codoped $K_2B_4O_7$:Dy^{3+} as an efficient and structurally tunable borate-based phosphor.

Table 6
Experimentally derived branching ratios (β) for the $^4F_{9/2} \rightarrow {}^6H_J$ and ^6F_J emissions of Dy^{3+} in $K_2B_4O_7$ and Li^+ -codoped $K_2B_4O_7$. The β values were calculated by normalizing the integrated emission intensities of each transition.

(a) $K_2B_4O_7$:0.03Dy^{3+}

Transition	λ (nm)	Peak Area	β
$^4F_{9/2} \rightarrow {}^6H_{15/2}$	482	1,346,238.990	0.303
$^4F_{9/2} \rightarrow {}^6H_{13/2}$	576	2,455,979.618	0.553
$^4F_{9/2} \rightarrow {}^6H_{11/2}$	644	164,622.552	0.037
$^4F_{9/2} \rightarrow {}^6F_{11/2}/{}^6H_{9/2}$	758	481,588.131	0.108

(b) $K_2B_4O_7$:0.03Dy^{3+},0.01Li^+

Transition	λ (nm)	Peak Area	β
$^4F_{9/2} \rightarrow {}^6H_{15/2}$	482	3,468,079.645	0.317
$^4F_{9/2} \rightarrow {}^6H_{13/2}$	576	5,999,976.918	0.548
$^4F_{9/2} \rightarrow {}^6H_{11/2}$	644	467,056.607	0.043
$^4F_{9/2} \rightarrow {}^6F_{11/2}/{}^6H_{9/2}$	758	795,104.709	0.072

Table 7
Judd–Ofelt intensity parameters (Ω_2, Ω_4, Ω_6) of Dy^{3+} ions in $K_2B_4O_7$ and Li^+ -codoped $K_2B_4O_7$ phosphors.

Sample	Ω_2 ($\times 10^{-20}$ cm^2)	Ω_4 ($\times 10^{-20}$ cm^2)	Ω_6 ($\times 10^{-20}$ cm^2)
$K_2B_4O_7$:0.03Dy^{3+}	1.38	0.92	4.87
$K_2B_4O_7$:0.03Dy^{3+},0.01Li^+	1.61	1.05	5.21

Table 8
Radiative lifetime (τ_{rad}) and internal quantum efficiency (η) of Dy^{3+} ions in $K_2B_4O_7$ and Li^+ -codoped $K_2B_4O_7$.

Sample	τ_1 (μs)	τ_2 (μs)	τ_{avg} (μs)	τ_{rad} (μs)	η (%)
$K_2B_4O_7$:0.03Dy^{3+}	25.796	1629.063	1589.386	~1900	83.6
$K_2B_4O_7$:0.03Dy^{3+},0.01Li^+	39.276	2537.657	2516.846	~2600	96.8

3.6. CIE chromaticity analysis

The CIE 1931 chromaticity coordinates of the $K_2B_4O_7$:xDy^{3+} phosphors exhibit a systematic evolution with Dy^{3+} concentration, reflecting the relative contributions of the blue ($^4F_{9/2} \rightarrow {}^6H_{15/2}$) and yellow ($^4F_{9/2} \rightarrow {}^6H_{13/2}$) emissions. As shown in the CIE diagram (see Fig. 10), all samples lie within the near-white region, with coordinates clustering between $x = 0.29$–0.35 and $y = 0.27$–0.35, indicating the coexistence of both emission channels. Increasing Dy^{3+} content initially shifts the coordinates toward higher x and y values (samples A–C), driven by the strengthening of the yellow transition. At higher concentrations, concentration quenching suppresses the yellow band to some extent, resulting in a slight movement toward lower x and y values (samples E–F). This progression confirms that Dy^{3+} concentration governs the balance between blue and yellow emissions and thereby modulates the chromaticity.

Li^+ co-doping produces a distinct modification of the chromaticity behavior. The CIE coordinates of $K_2B_4O_7$:0.03Dy^{3+},yLi^+ shift upward in the diagram, with y increasing from 0.3422 (undoped) to 0.4055 at $y = 0.005$, indicating an enhancement of the yellow ($^4F_{9/2} \rightarrow {}^6H_{13/2}$) emission. This trend reflects the increased local asymmetry around Dy^{3+} ions induced by Li^+ incorporation, consistent with the rise in Ω_2 and the elevated radiative efficiency. Although further Li^+ addition tends to moderate this shift, the chromaticity points remain clustered in the warm-white region, demonstrating that Li^+ enhances the electric-dipole character of Dy^{3+} without destabilizing the overall emission balance.

In contrast, Na^+ co-doping induces a downward shift in the CIE diagram, with both x and y values decreasing progressively with increasing Na^+ content. For instance, the coordinates shift from (0.3472, 0.3422) for the Dy^{3+}-doped sample without alkali co-dopant to (0.2748, 0.2285) at a Na^+ concentration of y = 0.07. This movement toward the blue-cyan region indicates that Na^+ co-doping suppresses the yellow transition more strongly than Li^+ co-doping, likely due to the weaker polarizability of Na^+ and its reduced ability to modify the Dy^{3+}–O^{2-} coordination environment. The observed trend matches the reduction in radiative efficiency and the diminution of hypersensitive transition strength identified in the Judd–Ofelt analysis.

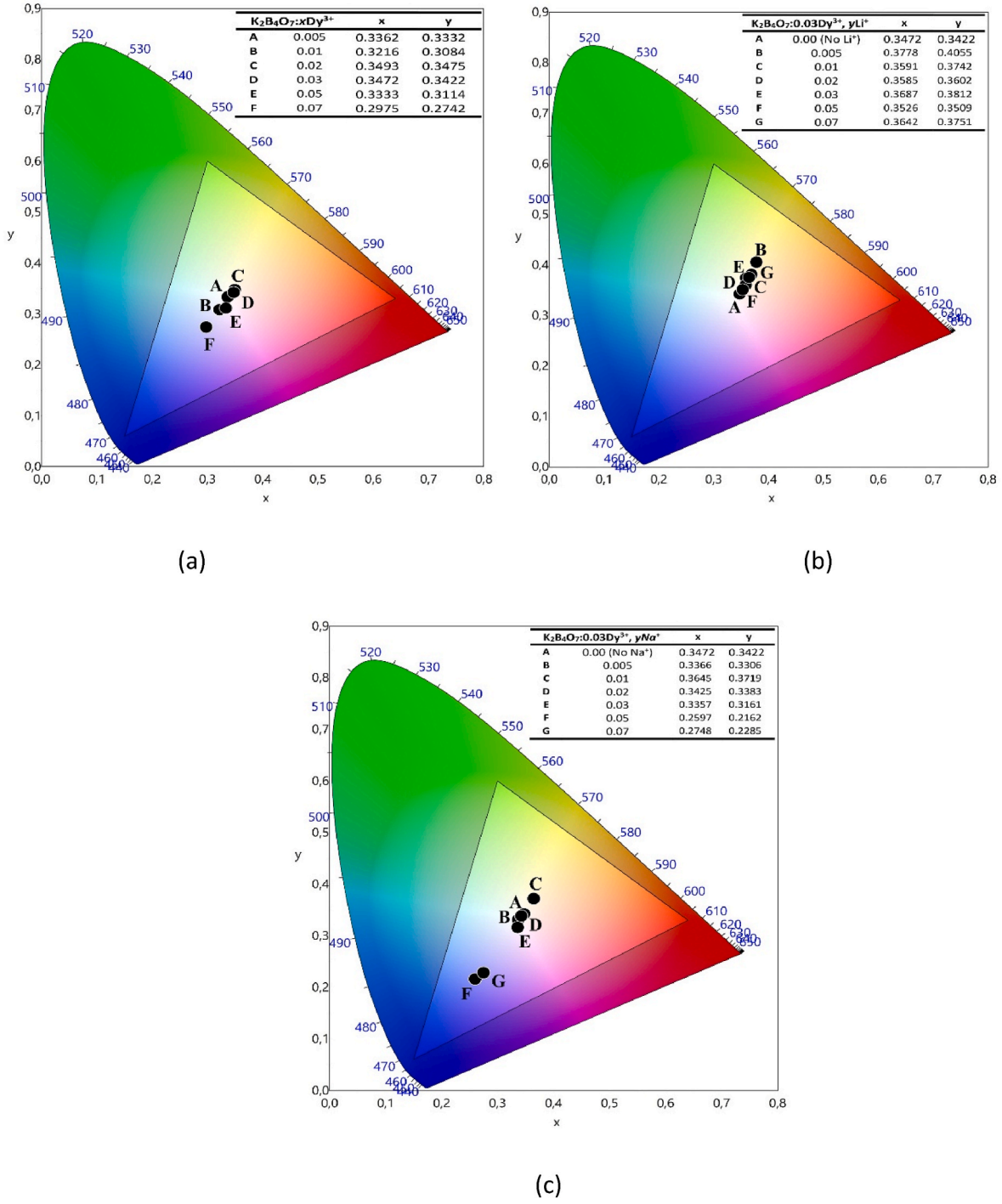

Fig. 10. CIE 1931 chromaticity coordinates of the synthesized phosphors: (a) $K_2B_4O_7$:xDy^{3+}, (b) $K_2B_4O_7$:0.03Dy^{3+},yLi^{+}, and (c) $K_2B_4O_7$:0.03Dy^{3+},yNa^{+}.

Overall, the chromaticity results confirm that Dy^{3+} concentration and alkali-ion co-doping provide effective means to tune the emission color of $K_2B_4O_7$-based phosphors. Li^{+} co-doping shifts the emission toward warmer white shades by promoting electric-dipole activity, whereas Na^{+} co-doping drives the coordinates toward cooler tones by diminishing the yellow-channel contribution. These trends are consistent with the optical lifetime, branching ratio, and Judd–Ofelt parameter analyses, collectively demonstrating the structural and spectroscopic tunability of the $K_2B_4O_7$ host lattice.

4. Conclusions

In this work, the structural and optical characteristics of Dy^{3+}-activated $K_2B_4O_7$ and its Li^{+}/Na^{+} codoped derivatives were comprehensively investigated to elucidate the impact of charge compensation on emission behavior. This study emphasizes host-specific physicochemical regulation rather than a generic alkali-ion co-doping effect. Structural analyses confirmed that Dy^{3+} incorporation and alkali-ion co-doping preserve the orthorhombic host lattice while introducing subtle modifications in the Dy^{3+}–O^{2-} coordination environment. These changes are reflected in the vibrational response and microstructural uniformity, indicating that the tetraborate network is capable of accommodating

both activator and co-dopant ions. Optical measurements revealed strong Dy^{3+} emissions with an optimal concentration of 3 wt%. Li^+ co-doping markedly enhanced the luminescence output by reducing defect-induced quenching and improving lattice coherence, whereas Na^+ co-doping resulted in comparatively weaker reinforcement. Temperature-dependent photoluminescence highlighted the exceptional thermal robustness of the host matrix and revealed pronounced anti-thermal-quenching behavior preferentially induced by Li^+ co-doping, with emission intensity increasing over the 300–550 K temperature range. Importantly, the extracted activation energy for thermal quenching ($E_a \approx 0.21$ eV) is significantly higher than values reported for many Dy^{3+}-based phosphors, underscoring the strong resistance of the system to thermally driven non-radiative processes. Judd–Ofelt analysis showed that Li^+ co-doping increases the Ω_2, Ω_4 and Ω_6 intensity parameters, indicating enhanced asymmetry and strengthened electric-dipole interactions. This enhancement results in higher radiative probabilities and a substantial increase in internal quantum efficiency. By correlating charge compensation, local-field modulation, and thermal stability, this work establishes a quantitative structure–property–performance design guideline for rare-earth-doped tetraborate phosphors, positioning Li^+-modified $K_2B_4O_7$:Dy^{3+} as a promising phosphor platform for high-temperature and high-power solid-state lighting applications. The tunable CIE chromaticity coordinates, spanning near-white to warm-white regions, further highlight the versatility of the system. Overall, the combination of high activation energy, excellent thermal stability, improved dipole strength, and composition-dependent color tunability establishes Li^+-modified $K_2B_4O_7$:Dy^{3+} as a promising phosphor platform for high-temperature and high-power solid-state lighting technologies.

CRediT authorship contribution statement

M.B. Coban: Software, Methodology, Investigation, Funding acquisition. **Abeer S. Altowyan:** Writing – original draft, Methodology, Investigation, Funding acquisition, Formal analysis. **U.H. Kaynar:** Software, Methodology, Investigation, Funding acquisition, Formal analysis. **Jabir Hakami:** Investigation, Conceptualization. **H. Aydin:** Software, Methodology, Investigation. **I. Kara:** Software, Methodology, Investigation. **A. Canimoglu:** Methodology, Investigation, Conceptualization. **N. Can:** Writing – review & editing, Writing – original draft, Supervision.

Declaration of competing interest

The authors declare that they have no known competing financial interests or personal relationships that could have appeared to influence the work reported in this paper.

Acknowledgements

The authors acknowledge the financial support provided by the Research Funds of Balikesir University (Grant No. BAP-2025/099). The authors also acknowledge the Princess Nourah bint Abdulrahman University Researchers Supporting Project (Project No. PNURSP2026R16), Princess Nourah bint Abdulrahman University, Riyadh, Saudi Arabia. This study was further supported by the Scientific and Technological Research Council of Turkey (TÜBİTAK) under Project No. 223M036.

References

[1] A. Tiwari, S.J. Dhoble, Borate-based luminescent materials: a comprehensive review of structural influences on thermal stability and luminescence characteristics, J. Lumin. 287 (2025) 121490, https://doi.org/10.1016/j.jlumin.2025.121490.
[2] D.P. Awade, Borate phosphors for solid-state lighting, in: Borate Phosphors, CRC Press, Boca Raton, 2022, pp. 75–106, https://doi.org/10.1201/9781003207757-4.
[3] S. Verma, K. Verma, D. Kumar, B. Chaudhary, S. Som, V. Sharma, V. Kumar, H. C. Swart, Recent advances in rare earth doped alkali-alkaline earth borates for solid state lighting applications, Phys. B Condens. Matter 535 (2018) 106–113, https://doi.org/10.1016/j.physb.2017.06.073.
[4] I.I. Kindrat, B.V. Padlyak, B. Kukliński, A. Drzewiecki, V.T. Adamiv, Enhancement of the Eu^{3+} luminescence in $Li_2B_4O_7$ glasses co-doped with Eu and Ag, J. Lumin. 204 (2018) 122–129, https://doi.org/10.1016/j.jlumin.2018.07.051.
[5] B.V. Padlyak, I.I. Kindrat, V.T. Adamiv, A. Drzewiecki, I. Stefaniuk, Spectroscopic properties and photoluminescence of the $Li_2B_4O_7$:Mn,Sm glass, Mater. Res. Bull. 175 (2024) 112788, https://doi.org/10.1016/j.materresbull.2024.112788.
[6] I.I. Kindrat, B.V. Padlyak, A. Drzewiecki, Luminescence properties of the Sm-doped borate glasses, J. Lumin. 166 (2015) 264–275, https://doi.org/10.1016/j.jlumin.2015.05.051.
[7] F.B. Xiong, H.F. Lin, Y.C. Xu, H.X. Shen, W.Z. Zhu, New thermally stable red-emitting phosphors Pr^{3+}, M+:SrB_4O_7 (m=Li, Na, K), J. Lumin. 177 (2016) 99–103, https://doi.org/10.1016/j.jlumin.2016.04.035.
[8] Tejas, A. Princy, S.M. Moses Kennedy, M.I. Sayyed, T.A. Hanafy, S.D. Kamath, Structural, optical, and thermal traits of Sm^{3+}-doped SrB_2O_4 phosphors for solid-state lighting applications, Solid State Sci. 157 (2024) 107724, https://doi.org/10.1016/j.solidstatesciences.2024.107724.
[9] R. Hemam, L.R. Singh, S.D. Singh, R.N. Sharan, Preparation of CaB_4O_7 nanoparticles doped with different concentrations of Tb^{3+}:Photoluminescence and thermoluminescence/optically stimulated luminescence study, J. Lumin. 197 (2018) 399–405, https://doi.org/10.1016/j.jlumin.2018.01.062.
[10] R. Mohan P, S.K. Jose, A. George, N.V. Unnikrishnan, C. Joseph, P.R. Biju, Synthesis and photoluminescence characteristics of near white light emitting CaB_2O_4:Dy^{3+},Li^+ phosphor, J. Phys. Chem. Solids 119 (2018) 166–174, https://doi.org/10.1016/j.jpcs.2018.03.039.
[11] A.S. Altowyan, U.H. Kaynar, H. Aydin, J. Hakami, M.B. Coban, K. Cikrikci, M. Ayvacikli, N. Can, Synthesis, structural characterization, and photoluminescence properties of Dy^{3+}-Doped CaB_4O_7 phosphors: influence of Li^+ and K^+ Co-doping, Mater. Sci. Semicond. Process. 195 (2025) 109593, https://doi.org/10.1016/j.mssp.2025.109593.
[12] S. Jipa, W. Kappel, T. Zaharescu, L.M. Gorghiu, C. Dumitrescu, Activation energy from thermoluminescence of $K_2B_4O_7$ doped with Cu and Ag, Rev. Chim. 59 (2008) 300–303, https://doi.org/10.37358/RC.08.3.1752.
[13] Z. Xiong, Q. Tang, C. Zhang, Investigation of thermoluminescence in $Li_2B_4O_7$ phosphors doped with Cu, Ag and Mg, Sci. China Ser. G Physics, Mech. Astron. 50 (2007) 311–320, https://doi.org/10.1007/s11433-007-0020-3.
[14] S.K. Gupta, K. Sudarshan, A.K. Yadav, R. Gupta, D. Bhattacharyya, S.N. Jha, R. M. Kadam, Deciphering the role of charge compensator in optical properties of $SrWO_4$:Eu^{3+} :A (A = Li^+, Na^+, K^+): spectroscopic insight using photoluminescence, positron annihilation, and X-ray absorption, Inorg. Chem. 57 (2018) 821–832, https://doi.org/10.1021/acs.inorgchem.7b02780.
[15] H. Orucu, A.S. Altowyan, U.H. Kaynar, H. Aydin, M.B. Coban, J. Hakami, N. Can, Synthesis, structural characterization, and photoluminescence behavior of $NaCa_4(BO_3)_3$:Tb^{3+} phosphors Co-doped with K^+: insights into radiation-induced defect formation and charge compensation via DFT calculations, Appl. Radiat. Isot. 225 (2025) 112038, https://doi.org/10.1016/j.apradiso.2025.112038.
[16] E. Ekdal Karali, A.S. Altowyan, S. Yusan, H. Aydin, U.H. Kaynar, M.B. Coban, J. Hakami, E. Aymila Çin, T. Karman, A. Canimoglu, N. Can, Na+-driven enhancement of the $^5D_0 \rightarrow {}^7F_4$ emission in Eu^{3+}-activated $KCa_4(BO_3)_3$: photoluminescence and Judd–Ofelt studo, J. Photochem. Photobiol. Chem. 472 (2026) 116829, https://doi.org/10.1016/j.jphotochem.2025.116829.
[17] X.-Y. Sun, J.-C. Zhang, X.-G. Liu, L.-W. Lin, Enhanced luminescence of novel $Ca_3B_2O_6$:Dy^{3+} phosphors by Li^+-codoping for LED applications, Ceram. Int. 38 (2012) 1065–1070, https://doi.org/10.1016/j.ceramint.2011.08.032.
[18] S. Ponkumar, D. Prakashbabu, K. Parasuraman, R. Uthrakumar, K. Kaviyarasu, Synthesis, characterization, and enhanced photoluminescence of ZrO_2:Dy^{3+} phosphors by incorporating Li^+, Na^+ and K^+ ions for LED applications, Ceram. Int. 50 (2024) 13219–13228, https://doi.org/10.1016/j.ceramint.2024.01.233.
[19] L. Jun, X. Shuping, G. Shiyang, FT-IR and raman spectroscopic study of hydrated borates, Spectrochim. Acta Part A Mol. Biomol. Spectrosc. 51 (1995) 519–532, https://doi.org/10.1016/0584-8539(94)00183-C.
[20] G. Padmaja, P. Kistaiah, Infrared and raman spectroscopic studies on alkali borate glasses: evidence of mixed alkali effect, J. Phys. Chem. A 113 (2009) 2397–2404, https://doi.org/10.1021/jp809318e.
[21] M.A. Morsy, T.F. Garrison, M.R. Kessler, M.H.A. Mhareb, H.Z. El-Deen, Structural elucidation of lithium borate glasses using XRD, FTIR, and EPR spectroscopy, ACS Phys. Chem. Au 5 (2025) 227–238, https://doi.org/10.1021/acsphyschemau.4c00106.
[22] S. Iflazoglu, First-time synthesis and investigation of structural and optical properties of Dy^{3+} doped $Ba_3(BO_3)_2$, J. Mol. Struct. 1348 (2025) 143447, https://doi.org/10.1016/j.molstruc.2025.143447.
[23] H. Liu, Q. Liu, Y. Lan, D. Wang, L. Zhang, X. Tang, S. Yang, Z. Luo, G. Tian, Speciation of borate in aqueous solutions studied experimentally by potentiometry and raman spectroscopy and computationally by DFT calculations, New J. Chem. 47 (2023) 8499–8506, https://doi.org/10.1039/D3NJ00751K.
[24] F. Yang, H. Ma, Y. Liu, B. Han, H. Feng, Q. Yu, Photoluminescence properties of novel Dy^{3+} doped $Ba_5CaAl_4O_{12}$ phosphors, Ceram. Int. 40 (2014) 10189–10192, https://doi.org/10.1016/j.ceramint.2014.02.068.
[25] G. Blasse, B.C. Grabmaier, Luminescent Materials, Springer Berlin Heidelberg, Berlin, Heidelberg, 1994, https://doi.org/10.1007/978-3-642-79017-1.
[26] Y. Li, Y. Hao, Energy transfer-enabled color-tunable single-phase phosphor for highly white leds and optical anti-counterfeiting. https://doi.org/10.2139/ssrn.5379026, 2025.

[27] R.A. Penneman, R.R. Ryan, A. Rosenzweig, R. Reisfeld, J. Felsche, C.K. Jørgensen, Rare Earths, Springer Berlin Heidelberg, Berlin, Heidelberg, 1961, https://doi.org/10.1063/1.3057544.
[28] K. Poria, R. Lohan, S. Bhatia, A. Kumar, R. Singh, N. Deopa, R. Punia, J.S. Shahi, A. S. Rao, Lumino-structural properties of Dy^{3+} activated $Na_3Ba_2LaNb_{10}O_{30}$ phosphors with enhanced internal quantum yield for w-LEDs, RSC Adv. 13 (2023) 11557–11568, https://doi.org/10.1039/D3RA01260C.
[29] R. Cao, L. Su, X. Cheng, T. Chen, W. Li, H. Ao, S. Guo, G. Zheng, Preparation and photoluminescence properties of $LaBMoO_6$:Dy^{3+} yellow-emitting phosphor for LEDs, Appl. Phys. A 125 (2019) 233, https://doi.org/10.1007/s00339-019-2511-2.
[30] C. Zhang, Y. Chen, S. Ma, H. Fan, Y. Yu, Z. Hu, N. Ye, J. Wang, Y. Wu, Effective warm white-light emission with Dy:$YAlO_3$ single crystal, Chinese Opt. Lett. 21 (2023) 051602.
[31] E. Cavalli, (INVITED) optical spectroscopy of Dy^{3+} in crystalline hosts: general aspects, personal considerations and some news, Opt. Mater. X 1 (2019) 100014, https://doi.org/10.1016/j.omx.2019.100014.
[32] R. Reisfeld, C.K. Jørgensen, Lasers and Excited States of Rare Earths, Springer Berlin Heidelberg, Berlin, Heidelberg, 1977, https://doi.org/10.1007/978-3-642-66696-4.
[33] G. Blasse, Energy transfer in oxidic phosphors, Phys. Lett. 28 (1968) 444–445, https://doi.org/10.1016/0375-9601(68)90486-6.
[34] X. Qin, X. Zhang, P. He, Q. Pang, L. Zhou, M. Gong, Enhanced luminescence properties and energy transfer in Ce^{3+} and Tb^{3+} co-doped NaCaBO3 phosphor, Ceram. Int. 41 (2015) 5554–5560, https://doi.org/10.1016/j.ceramint.2014.12.132.
[35] F. Zhao, P. Guo, G. Li, F. Liao, S. Tian, X. Jing, Luminescent properties of Eu^{3+}, Tb^{3+} or Bi^{3+} activated yttrium germanates, Mater. Res. Bull. 38 (2003) 931–940, https://doi.org/10.1016/S0025-5408(03)00086-2.
[36] D.L. Dexter, A theory of sensitized luminescence in solids, J. Chem. Phys. 21 (1953) 836–850, https://doi.org/10.1063/1.1699044.
[37] L.G. Van Uitert, Characterization of energy transfer interactions between rare Earth ions, J. Electrochem. Soc. 114 (1967) 1048, https://doi.org/10.1149/1.2424184.
[38] P. Singh, H. Mishra, S.B. Rai, Multicolor tunable emission through energy transfer in Dy^{3+}/Ho^{3+} co-doped $CaTiO_3$ phosphors with high thermal stability for solid state lighting applications, Sci. Rep. 13 (2023) 21221, https://doi.org/10.1038/s41598-023-46065-4.
[39] R. Yantake, M. Kaiheriman, T. Yusufu, A. Sidike, Effect of Li^+ doping on the luminescence performance of a novel $KAlSiO_4$:Tb^{3+} green-emitting phosphor, Sci. Rep. 11 (2021) 5123, https://doi.org/10.1038/s41598-021-84220-x.
[40] A. Tyagi, M. Rakshita, D. Haranath, C. Shivakumara, Thermally stable Li^+ co-doped $ZnMoO_4$:Eu^{3+} phosphors for white LEDs, nitroaromatic sensing and low temperature non-contact optical thermometry applications, Mater. Adv. 6 (2025) 5758–5776, https://doi.org/10.1039/D5MA00280J.
[41] A.S. Altowyan, U.H. Kaynar, E.A. Çin, T. Karaman, H. Aydin, M.B. Coban, J. Hakami, N. Can, Eu^{3+} and Li^+ Co-doped $SmCa_4O(BO_3)_3$ phosphors: negative thermal quenching and photoluminescence properties, J. Alloys Compd. 1021 (2025) 179766, https://doi.org/10.1016/j.jallcom.2025.179766.
[42] G. Souadi, U.H. Kaynar, M. Ayvacikli, A. Canimoglu, N. Can, Synthesis and enhanced photoluminescence of the $BaSiF_6$:Dy^{3+} phosphors by Li^+ doping via combustion method, J. Lumin. 241 (2022) 118512, https://doi.org/10.1016/j.jlumin.2021.118512.
[43] T. Wang, W. Zhang, X. Wang, X. Huang, P. Zhang, $Ca_{19}Zn_2(PO_4)_{14}$:Dy^{3+}, M^+ (M = Li, Na, K) white-emitting phosphors: charge compensation effect of M+ on the photoluminescence enhancement, Ceram. Int. 47 (2021) 14260–14269, https://doi.org/10.1016/j.ceramint.2021.01.289.
[44] S. Liu, S. Liu, J. Wang, P. Sun, Y. Zhong, J.H. Jeong, B. Deng, R. Yu, Preparation and investigation of Dy^{3+}-doped $Ca_9LiGd_{2/3}(PO_4)_7$ single-phase full-color phosphor, Mater. Res. Bull. 108 (2018) 275–280, https://doi.org/10.1016/j.materresbull.2018.08.026.
[45] G. Zhang, L. Zhao, F. Fan, Y. Bai, B. Ouyang, W. Chen, Y. Li, L. Huang, Near UV-pumped yellow-emitting Ca_3TeO_6:Dy^{3+} phosphor for white light-emitting diodes, Spectrochim. Acta Part A Mol. Biomol. Spectrosc. 223 (2019) 117343, https://doi.org/10.1016/j.saa.2019.117343.
[46] J. Guo, S. Li, J. Kong, Y. Li, L. Zhou, L. Lou, Q. Lv, R. Tang, L. Zheng, B. Deng, R. Yu, Synthesis and characterization of a new double perovskite phosphor: $NaCaTiTaO_6$:Dy^{3+} with high thermal stability for w-LEDs application, Opt. Laser Technol. 155 (2022) 108347, https://doi.org/10.1016/j.optlastec.2022.108347.
[47] J. Hakami, U.H. Kaynar, M.B. Coban, H. Aydin, R. Alamri, D.A. Jabali, N. Can, Optical performance and luminescence properties of Dy^{3+}-doped $LaMgB_5O_{10}$ phosphors, Inorg. Chem. Commun. 171 (2025) 113540, https://doi.org/10.1016/j.inoche.2024.113540.